Seasonality of meridional overturning in the subpolar North Atlantic: ~~implications for relying on the streamfunction maximum density flux~~ as a metric ~~of~~ for understanding AMOC~~slowdown~~

Alan D. Fox[1], Neil J. Fraser[1], and Stuart A. Cunningham[1]

[1]Scottish Association for Marine Science, Oban, UK

Correspondence: Alan D. Fox (alan.fox@sams.ac.uk)

Abstract.

Atlantic meridional overturning circulation has a notable seasonal component. This influences the jet stream and the location, frequency and intensity of extreme weather events. Understanding this seasonality is important for mitigating the impacts of AMOC changes on European weather and climate. Here we place meridional overturning and fluxes in a coherent framework. This framework highlights the integral relationship between meridional overturning circulation and property transports, both being functions purely of the overturning streamfunction Ψ. Using this framework we examine the seasonality observed in overturning and density, temperature and freshwater fluxes at the OSNAP line in the subpolar North Atlantic. We find the seasonal cycle of the MOC metric (the standard measure of overturning defined as the maximum of the overturning streamfunction) to be dominated by Ekman transports and the large-scale seasonal cycle of surface density; heat flux to be dominated by barotropic velocity variability; the seasonal cycle of freshwater flux by a combination of barotropic velocities and the salinity in the western boundary current; and density flux to reflect a broad range of characteristics and processes. We show that the MOC metric is a poor predictor, on seasonal time-scales, of either density fluxes or the more societally relevant ocean heat and freshwater transports. This is due to each of these metrics responding to different physical processes. The MOC metric, on seasonal timescales at least, has very high sensitivity to near-surface physical characteristics in a limited geographical area. These characteristics are not necessarily reflective of the fundamental processes driving overturning. Therefore, we suggest caution in the use of the standard MOC metric when studying overturning, and the routine use of the density flux as a valuable additional overturning metric.

1 Introduction

Atlantic meridional overturning circulation (AMOC) has a notable seasonal component. This influences the jet stream and the location, frequency and intensity of extreme weather events. Understanding this seasonality is important for mitigating the impacts of AMOC changes on European weather and climate. Driven by innovation in ocean observation, theory and modelling our understanding of subpolar North Atlantic meridional overturning has advanced rapidly in recent years. Basin-wide observational arrays, particularly OSNAP (Overturning in the Subpolar North Atlantic Program, Lozier et al., 2019), now allow robust estimation of the seasonal cycle in the strength of subpolar overturning and associated heat and freshwater transports (Gary

et al., 2018; Fu et al., 2023; Fraser et al., 2024; Mercier et al., 2024). Theoretical models of overturning (see Johnson et al., 2019, for a review of the state of the art) help us understand the interplay between surface buoyancy and wind forcing, and provide new paradigms for deep water formation. Coupled models (e.g. Swingedouw et al., 2007; Böning et al., 2016; Weijer et al., 2020; Baker et al., 2 help to better understand AMOC feedback mechanisms between ocean and atmosphere, generally predicting AMOC weakening during the twenty-first century, driven by freshwater input and reduced surface cooling – though results still vary widely. Mean-while global-scale high resolution ocean models (e.g. Hirschi et al., 2020; Biastoch et al., 2021), and state estimates (Forget et al., 2015) allow us to make detailed examination of fine-scale dynamics and mechanisms driving AMOC variability at shorter timescales.

While the driving processes of Atlantic meridional overturning circulation (AMOC) – winds, surface fluxes and freshwater input – have marked seasonal cycles at subpolar latitudes, it remains unclear how, or if, these seasonal cycles are expressed in the observations of AMOC and related transports on basin-wide sections such as OSNAP. Observational and modelling studies of subpolar North Atlantic meridional overturning consistently return estimates of the seasonal cycle of overturning, as measured by the maximum of the overturning streamfunction (MOC_σ), with amplitude of about $4\,\mathrm{Sv}$ with a late spring maximum and autumn or winter minimum (Lozier et al., 2019; Fu et al., 2023; Wang et al., 2021; Tooth et al., 2023; Mercier et al., 2024). These studies find overturning seasonality, as for the mean subpolar overturning (Lozier et al., 2019; Petit et al., 2020), to be dominated by water transformation north of a line linking Greenland and Scotland rather than in the Labrador Sea.

Analyses of OSNAP observations (Fu et al., 2023) show the subpolar AMOC seasonal cycle to be dominated by seasonality in the Irminger Basin, particularly the East Greenland Current, modified by Ekman transport driven by seasonality in the zonal winds. The East Greenland Current seasonality is ascribed to a lagged signal of watermass transformation in the Irminger Basin. Examination of an ocean reanalysis (Wang et al., 2021) and detailed observations (Le Bras et al., 2020) suggest the seasonal cycle of overturning closely follows *density variability* in the western boundary current. However, other observations show (Mercier et al., 2024; Le Bras et al., 2018) the *seasonal transport variability* in the western boundary current also to be an important contributor to AMOC seasonal cycle. The combined effect of density and transport seasonality is explored in results from a high resolution ocean hindcast model (Tooth et al., 2023), with innovative use of Lagrangian tracking used to attribute transport variability to variability of particle transit times round the northern subpolar Gyre. Seasonality in zonal winds is a common theme dominating MOC seasonality at lower latitudes (Yang, 2015; Zhao and Johns, 2014), with geostrophic transport at the boundaries and in the interior, perhaps in turn driven by wind-stress curl or a lagged response to deep-water formation, controlling the seasonal cycle at higher latitudes (Chidichimo et al., 2010; Zhao and Johns, 2014; Gary et al., 2018; Tooth et al., 2023; Mercier et al., 2024).

The maximum of the overturning streamfunction, integrated across the width of the basin and calculated variously in density (MOC_σ) or depth (MOC_z) space, has become synonymous with the strength of the meridional overturning circulation on a given transatlantic section. Indeed we will use it in this sense in the current work. In a wider, ocean conveyor-belt, sense, in the North Atlantic and Arctic basins the meridional overturning circulation is fundamentally a water transformation process – lighter surface waters flowing north, being transformed to denser waters, sinking, mixing and flowing south. Observational arrays such as OSNAP (Lozier et al., 2019) and RAPID (Cunningham et al., 2007; Kanzow et al., 2007) attempt to quantify

these transformation processes by monitoring the north-south exchanges along basin-wide sections. On shorter, seasonal and inter-annual, timescales it is clear that the 'overturning' signal observed at these arrays does not purely represent this wider, large-scale, overturning. Adiabatic, 'sloshing' motions (Han, 2023b, a; Fraser et al., 2025) driven by Ekman transport and wind-stress curl (Fraser et al., 2024) dominate observed MOC_σ on shorter timescales. Seasonal cycles of surface mixed layer warming and cooling, deepening and shallowing will also be expressed in the seasonal cycle of the overturning streamfunction, even where these changes are not ultimately subducted into the ocean interior and the overturning circulation (Tooth et al., 2023).

Here we attempt to disentangle the various processes expressed in the MOC_σ and overturning streamfunction at the OS-NAP line. To do this we adopt and extend the formalism proposed by Mercier et al. (2024). This formalism allows us to separate out components of the overturning streamfunction seasonal variability associated with, for example, surface Ekman transports, water transformation or velocity variability. We use these methods to examine the seasonal cycle in the full density-space overturning streamfunction, rather than focussing exclusively on MOC_σ (the maximum of the streamfunction). We ~~advocate for the routine use of the northward density flux(e.g. Fraser and Cunningham, 2021), which we show can be~~ also introduce an additional metric based on the overturning streamfunction, the 'density flux', calculated as the area under the overturning streamfunction curve ~~, as an additional metric alongside the MOC to give a more complete understanding of overturning~~(e.g. Fraser and Cunningham, 2021). This density flux is a somewhat neglected part of the watermass transformation theory (Tziperman, 1986; Speer and Tziperman, 1992; Nurser et al., 1999) which fundamentally underpins the concept of overturning, and has close parallels with both heat and freshwater transports. The density flux arises from mass conservation, rather than volume conservation as for MOC_σ, with density flux northward across a meridional section largely balanced by total surface density fluxes over the region north of the section in the longer term. This contrasts with MOC_σ which balances surface fluxes over the narrow outcrop region of a single isopycnal and diapycnal mixing across that isopycnal. Thus, density flux complements MOC_σ to give a more complete understanding of overturning. Using this framework, beginning with analysis of the output of a high-resolution model hindcast, we aim to produce a more comprehensive and integrated description of the seasonal cycle of overturning observed on the OSNAP line, encompassing MOC_σ, density flux, and heat and freshwater transports. We consider how each of these important overturning metrics responds differently to the underlying mechanisms driving the overturning. The model-derived hypotheses obtained are then tested against the seasonal cycle in the OSNAP observational timeseries, possible implications for AMOC and climate studies examining variability on longer timescales are discussed.

2 Methods

2.1 Data

We ~~conduct the model analysis using output from the 1/20°~~ make use of the eddy-rich, nested ocean–sea-ice model configuration VIKING20X~~JRA55-short model hindcast of the North Atlantic (Biastoch et al., 2021; Getzlaff and Schwarzkopf, 2024).~~, full details are given in Biastoch et al. (2021) and won't be repeated here, the data are available from Getzlaff and Schwarzkopf (2024)

. Briefly, in the vertical, VIKING20X uses 46 geopotential z-levels with layer thicknesses gradually increasing from 6 m at the surface to 250 m in the deepest layers. The bottom topography is represented by partially filled cells. In the horizontal, VIKING20X has a tripolar grid with 0.25°global resolution, which is refined in the Atlantic Ocean to 0.05°, yielding an effective grid spacing of 3 to 4 km in the subpolar North Atlantic. The run used here, VIKING20X-JRA-short, is an experiment forced from 1980 to 2019 by the JRA55-do forcing (version 1.4) (Tsujino et al., 2018). Hindcasts of the past 50–60 years in this eddy-rich configuration realistically simulate the large-scale horizontal circulation, including the AMOC, the distribution of the mesoscale, overflow, and convective processes, and the representation of regional current systems in the North and South Atlantic (Biastoch et al., 2021; Rühs et al., 2021). For consistency with the observations, we based our calculations on monthly mean model output. Model results presented in the main text are based on the final 20 years of this run, 2000 to 2019 (Supplementary Information contains results based on the 2014 to 2019 period to more closely match the observational period).

For the observational analysis we use the OSNAP 6-year gridded dataset and time series (Fu et al., 2023) and ERA5 surface wind stress ~~(?Hersbach et al., 2023)~~(Hersbach et al., 2020, 2023). For parts of the analysis we divide the OSNAP line at Greenland into OSNAP West (OSNAP$_W$) and OSNAP East (OSNAP$_E$). ERA5 wind stresses are interpolated onto the OSNAP gridded observation points and used to calculate Ekman transports across the OSNAP section. The location of the OSNAP section is shown in Fig. 1

2.2 Theoretical framework

The zonally integrated overturning streamfunction in density space, $\Psi_\sigma(\sigma, t)$, can be written:

$$\Psi_\sigma(\sigma, t) = \int_w^e \int_{\sigma_{\min}}^{\sigma} \iint_{R(\sigma, t)} v \frac{\partial z}{\partial \sigma}(x, z, t) \, d\sigma dz \, dx \tag{1}$$

where $R(\sigma, t)$ is the part of the (x, z) vertical plane defined by $\sigma_{min} < \sigma'(x, z, t) < \sigma$, that is, we integrate over the area with potential density less than σ. Here $x \in [w, e]$ is the along-section coordinate, $z \in [-H, \eta]$ is the vertical coordinate (positive upwards), and $v(x, z, t)$ is the velocity normal to the section at time t. The fixed horizontal section end points are given by w, e; $H(x)$ is the water depth; and $\eta(x, t)$ the sea surface height.

$$\tag{2}$$

~~where x is the along-section coordinate from minimum $(x = w)$ to maximum $(x = e)$, z is the vertical coordinate (positive upwards), v is the velocity normal to the section.~~ The overturning streamfunction Ψ has units of $\mathrm{m}^3\,\mathrm{s}^{-1}$, or more commonly Sv (Sverdrup, where $1\,\mathrm{Sv} = 1 \times 10^6\,\mathrm{m}^3\,\mathrm{s}^{-1}$). Note that we choose to integrate from low to high density. The direction of integration makes no difference when the total volume transport through the section is zero. On the OSNAP line there is generally a small net southward flow, integrating from high to low density then leads to small offsets in overturning and transports. Importantly for the work presented here the direction of integration has very little impact on the anomalies (~~zero~~no impact for the observations where net transports are fixed).
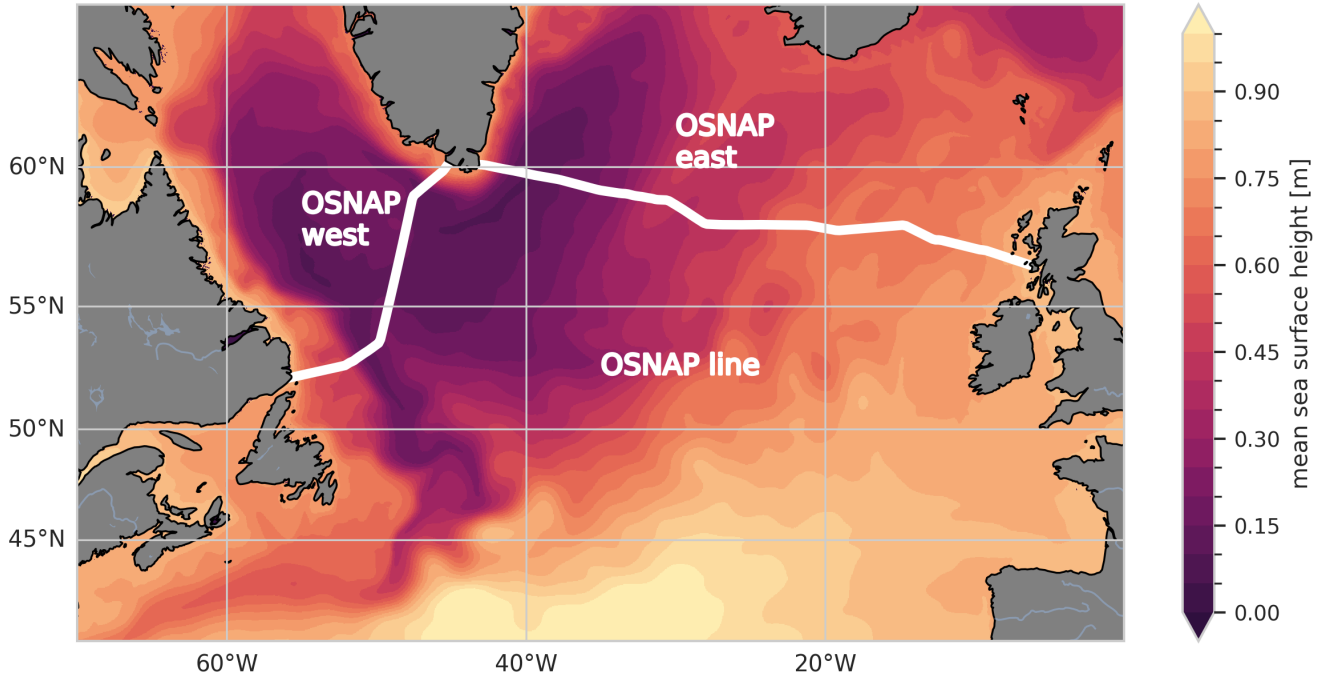
Figure 1. The location of the OSNAP observing line. We use OSNAP west to refer to the section across the Labrador Sea west of Greenland, and OSNAP east to refer to the section from Greenland to Scotland. The colour-scale represents the 20-year mean sea surface height from the VIKING20X model.

We then define~~the~~, in the usual way, the meridional overturning, $\mathrm{MOC}_\sigma(t)$, as the maximum of Ψ_σ for all σ, and $\sigma_{\mathrm{MOC}}(t)$
120   as the density at which this maximum occurs:

$$\mathrm{MOC}_\sigma(t) = \max_\sigma\left[\Psi_\sigma(\sigma,t)\right] \tag{3}$$

$$\sigma_{\mathrm{MOC}}(t) = \arg\max_\sigma\left[\Psi_\sigma(\sigma,t)\right] \tag{4}$$

~~The zonally and depth integrated~~ Here we introduce a further metric, the northward meridional density flux ($\mathcal{D}$)~~can be written~~:

125    $$\mathcal{D}(t) = -\int_w^e \int_{-H}^\eta v\sigma \frac{\sigma_{\max}}{\sigma_{\min}}\Psi_\sigma \, dz\,dx\,d\sigma \tag{5}$$

~~where H is the water depth and η the surface elevation~~This density flux forms a part of watermass transformation theory (Tziperman, 1986; Speer and Tziperman, 1992; Nurser et al., 1999), here we only consider the case where we integrate over

the full density range ($\sigma_{\min} < \sigma < \sigma_{\max}$). We follow convention in referring to this as 'density flux' while the units of $\mathrm{kg\,s^{-1}}$ perhaps suggest 'mass flux'. It is not a true mass flux as steric height changes are ignored in both model (via the Boussinesq approximation) and observational (surface defined as $z = 0$) calculations. The term 'density flux' captures the process intuitively – with lighter water flowing northwards and denser water returning southward being characterised as a southward (or negative northward) density flux. This metric is easily visualised as the area under the density-space streamfunction curves in Figs. 2 and 3.
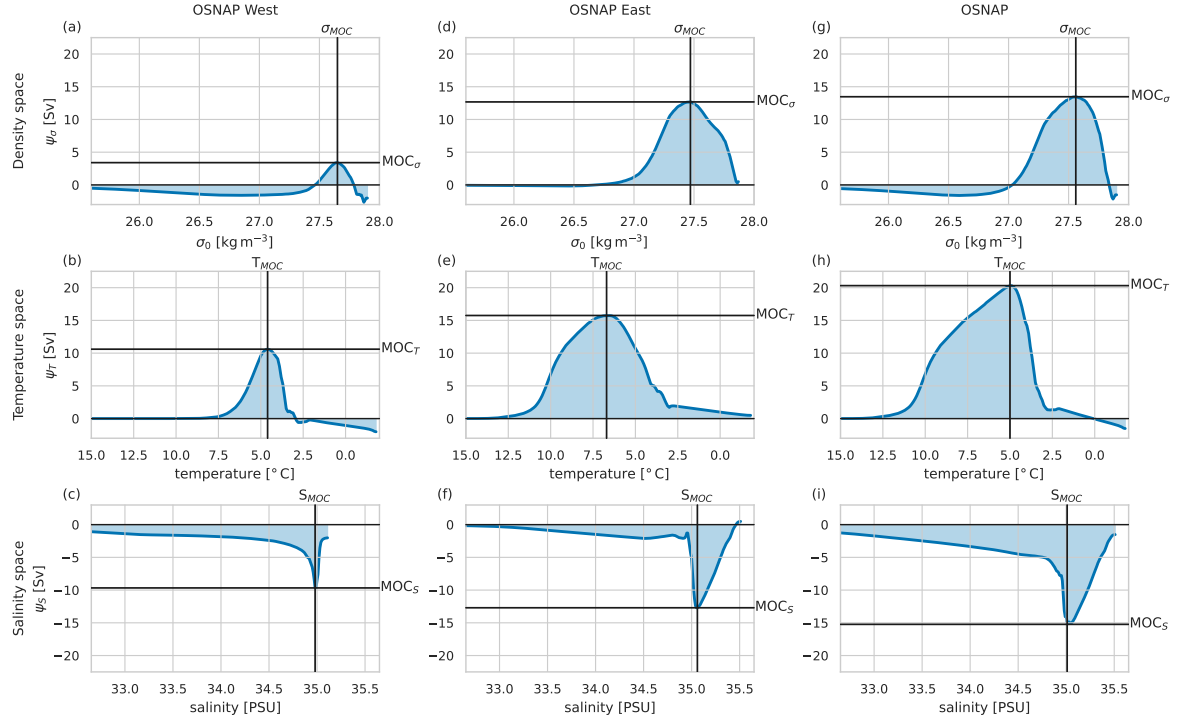
Figure 2. Mean overturning streamfunctions from 20-years of Viking20x model. The left-hand column (panels a-c) shows OSNAP$_\mathrm{W}$, the centre column (d-f) OSNAP$_\mathrm{E}$ and the right-hand column (g-i) the full OSNAP transect. In each case the top row (a,d,g) is the overturning streamfunction in density space, the middle row (b,e,h) in temperature space, and the bottom row (c,f,i) salinity space. The maximum overturning (negative in salinity space) is highlighted in each case, labelled MOC, along with the property value at which it occurs (σ_{MOC} for density, T_{MOC} for temperature, and S_{MOC} for salinity). The shaded integrated areas under the curve are proportional to the southward density flux (top row), the northward heat flux (middle row) and the northward freshwater flux (bottom row, negative shows net freshwater flux is southward). The plots are scaled such that unit area in each case very approximately corresponds to the same density flux – MOC$_\sigma$ and the southward density flux are a combination of northward heat flux opposed by southward freshwater flux.
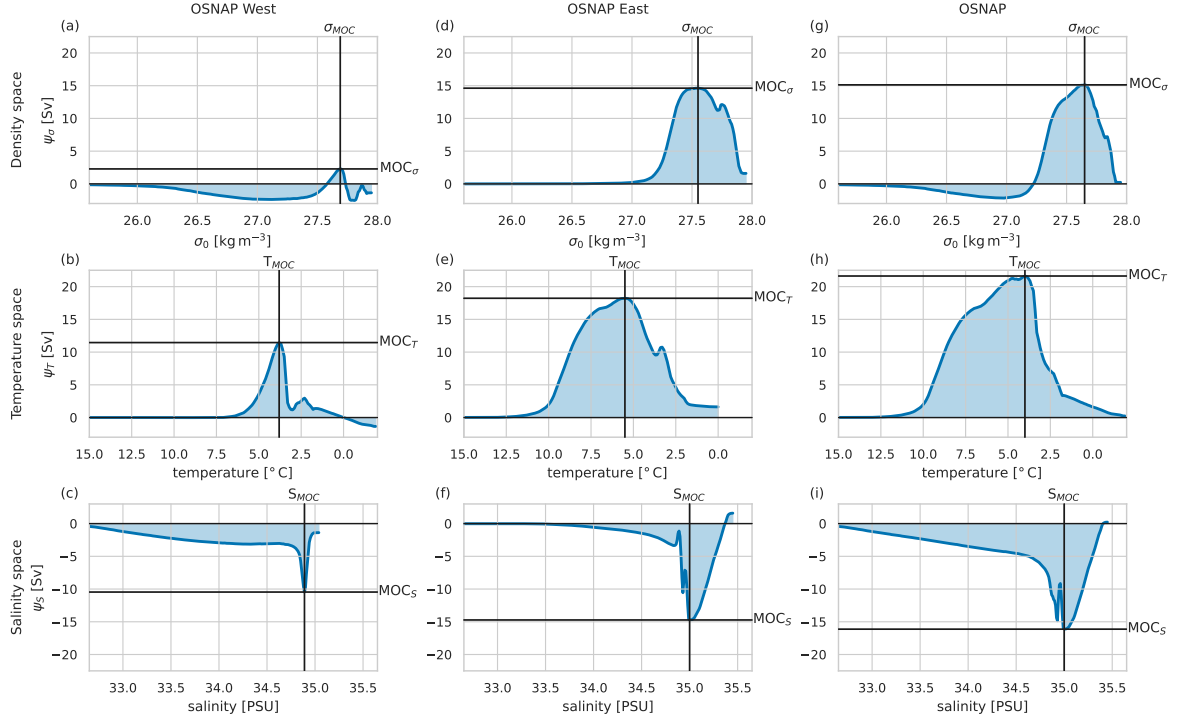
Figure 3. As for Fig. 2 but for the overturning from the 6-year OSNAP observational timeseries.

Rearranging Eq. ~~??~~5, we can write this density flux ~~as a function of the overturning streamfunction. Changing vertical coordinate from z to~~ and perhaps gain some physical insight. Changing coordinate from σ to z and integrating by parts, Eq. ~~??~~5 becomes:

$$\mathcal{D} = \sigma_{max} \int\limits_w^e \int\limits_{-H}^{\eta} \int\limits_{\sigma_{\min}}^{\sigma_{\max}} v \frac{\partial z}{\partial \sigma} d\sigma \, dz \, dx \; - \sigma_{max} \int\limits_w^e \Psi_\sigma \Big|_{\sigma_{\min}}^{\sigma_{\max}} \int\limits_{-H}^{\eta} v d\sigma \, dx \tag{6}$$

The ~~first~~ second term on the RHS of Eq. 6 is ~~just~~ a multiple of the net volume transport through the section. ~~For~~ If this net volume transport is zero - a useful approximation for the trans-ocean sections ~~and transport anomalies considered here this net volume transport is small and the first term can be ignored. So we have~~ considered here and one imposed in construction of the OSNAP observational overturning transports - the density flux ($\mathcal{D}$) reduces to simply the integral of $v\sigma$ over the section. If the net volume flux is non-zero however the RHS of Eq. 6 can become the difference between two large terms. We can further rewrite Eq. 6 as the integrated northward transport of density relative to reference density $\sigma_{\max}$:

$$\mathcal{D} = - \int_{\sigma_{\min}}^{\sigma_{\max}} \Psi_\sigma \, d_w^e \int_{-H}^{\eta} v(\sigma - \sigma_{\max}) \, dz \, dx \tag{7}$$

~~We have calculated the density flux using both Eqs. ?? and 5 and it makes no significant difference to our~~ For the streamfunction anomalies discussed here, all terms involving the reference density $\sigma_{\max}$ drop out for the observations as the net volume transport across each section is constant by construction. However, in the model the net volume transport varies in time (though is always small compared to the overturning transport). At the suggestion of an anonymous reviewer we repeated calculations after adding a uniform 'compensation' velocity to the model at each timestep to fix the net transports at their mean value. This made very little quantitative, and no qualitative, difference to the results.

A quick note on terminology. Throughout we use the terms 'overturning streamfunction' to refer to $\Psi(\sigma, t)$ and 'meridional overturning' or 'MOC' to refer to the maximum of Ψ in density space.

Note that the density-space equations have analogues in both temperature and salinity space, for the sake of brevity and clarity we will discuss temperature and salinity space results only briefly, and purely in the context of heat and freshwater transports, but the relevant equations are given here. In temperature, θ, space we have the overturning streamfunction (Ψ_θ), meridional overturning (MOC_θ at temperature θ_{MOC}), and meridional heat transport ($\mathcal{H}$). We choose to integrate downwards in temperature space, from high to low, which reverses the sign in the heat transport equation below.

$$\Psi_\theta(\theta, t) = \int_w^e \int_\theta^{\theta_{\max}} \iint_{R(\theta, t)} v \frac{\partial z}{\partial \theta}(x, z, t) \, d\theta \, dz \, dx, \quad \text{where } R(\theta, t) \text{ is the area defined by } \theta < \theta'(x, z, t) < \theta_{\max} \tag{8}$$

$$\mathrm{MOC}_\theta(t) = \max_\theta [\Psi_\theta(\theta, t)] \tag{9}$$

$$\theta_{\mathrm{MOC}}(t) = \arg\max_\theta [\Psi_\theta(\theta, t)] \tag{10}$$

$$\mathcal{H} = \rho \mathrm{C_p} \int_{\theta_{\min}}^{\theta_{\max}} \Psi_\theta \, d\theta \tag{11}$$

where ρ is potential density and $\mathrm{C_p}$ the specific heat capacity of sea water. Finally, in salinity, S, space we have the overturning streamfunction (Ψ_S), meridional overturning (MOC_S at salinity S_{MOC}), and northward meridional freshwater transport ($\mathcal{F}$). In salinity space the sign of the overturning streamfunction is usually reversed, with net freshwater input in the north opposing the overturning. So we define $\mathrm{MOC}_S(t)$ as the minimum of Ψ_S rather than the maximum. We also convert northward salinity transports to freshwater transports using a section mean reference salinity, $\overline{S}$. Hence,

$$\Psi_S(S,t) = \int\limits_{w}^{e} \int\limits_{S_{\min}}^{S} \iint_{R(S,t)} v\frac{\partial z}{\partial S}(x,z,t)\, dS\, dz\, dx, \quad \text{where } R(S,t) \text{ is the area defined by } S_{\min} < S'(x,z,t) < S \tag{12}$$

$$\mathrm{MOC}_S(t) = \min_S[\Psi_S(S,t)] \tag{13}$$

$$S_{\mathrm{MOC}}(t) = \operatorname*{arg\,min}_S[\Psi_S(S,t)] \tag{14}$$

$$\mathcal{F} = \frac{1}{S}\int\limits_{S_{\min}}^{S_{\max}} \Psi_S\, dS \tag{15}$$

170

These relationships are displayed graphically for the mean overturning streamfuctions in Figs. 2 and 3. Using this framework it becomes clear that ~~in each space MOC~~ the overturning and property transports metrics are intimately linked~~, one being the maximum and the other the integral of~~ . Considering density space, MOC is the extreme of the streamfunction Ψ, σ_{MOC} the position of that extreme, and density flux the area under the streamfunction curve. We can imagine scenarios in which variability

175 ~~of the two~~ these could be either strongly correlated ~~(e.g. a simple amplification of the flow),~~ or entirely decoupled~~(e.g. surface warming of upper limb water driving increased northward heat transport but having no effect on MOC).~~

~~Mean overturning streamfuctions from 20-years~~ : increasing the northward volume transport in the upper limb (and by extension the southward volume transport in the lower limb) would increase both MOC and density flux; but reducing the density of ~~Viking20x model. The left-hand column (panels a-c) shows OSNAP$_W$, the centre column (d-f) OSNAP$_E$ and~~

180 northward-flowing waters, say, would increase the area under the density flux, but MOC may be unaffected (the ~~right-hand column (g-i) the full OSNAP transect. In each case the top row (a,d,g) is the overturning streamfunction in density space, the middle row (b,e,h) in temperature space, and the bottom row (c,f,i) salinity space. The maximum overturning (negative in salinity space) is highlighted in each case, labelled~~ effect on MOC ~~, along with the property value at which it occurs (~~will depend on the density of the waters involved, and how that relates to σ_{MOC}~~for density , T_{MOC} for temperature, and S_{MOC} for~~

185 salinity). ~~The shaded integrated areas under the curve are proportional to the southward density flux(top row), the northward heat flux (middle row) and the northward freshwater flux (bottom row, negative shows net freshwater flux is southward). The plots are scaled such that unit area in each case very approximately corresponds to the same density flux — MOC$_\sigma$ and the southward density flux are a combination of northward heat flux opposed by southward freshwater flux.~~).

~~As for Fig. 2 but for the overturning from the 6-year OSNAP observational timeseries.~~

2.3 Streamfunction decomposition

190

We decompose the streamfunction variability into parts associated with velocity variability, density structure variability and co-variation of density and velocity fields ~~Mercier et al. (2024).~~ following Mercier et al. (2024). This decomposition helps us to examine the individual and combined influence on the seasonal cycle particular forcing, for example wind stress and surface density fluxes.

Rewriting Eq. 1 we have

$$\Psi_\sigma(\sigma, t) = \int\limits_w^e \int\limits_{z_\sigma(\sigma)}^{\underline{z_\sigma(0)}\,\eta} v(x, z, t)\, dz\, dx \tag{16}$$

where $\underline{z_\sigma(\sigma) = z_\sigma(\sigma, z, t)}\,z_\sigma(\sigma) = z_\sigma(\sigma, x, t)$ is the depth of the σ isopycnal at position x and time t.

We can decompose the velocity field into time-mean, $\overline{v}$, and variable, v', parts and the isopycnal depths into a time-mean part, $\overline{z}_\sigma$, and a deviation from the time-mean z'_σ. These time-means are calculated over the full length of the relevant dataset, so 6 years for the observations and 20 years for the model (6 years for the results from the shorter model timeseries included as SI).

$$v = \overline{v} + v' \tag{17}$$

$$z_\sigma = \overline{z}_\sigma + z'_\sigma. \tag{18}$$

We can then rewrite Eq. 16

$$\Psi_\sigma(\sigma, t) = \int\limits_w^e \int\limits_{\underline{\overline{z}_\sigma(\sigma) + z'_\sigma(\sigma)}\,\overline{z}_\sigma(\sigma) + z'_\sigma(\sigma, t)}^{\underline{z_\sigma(0)}\,\eta} \overline{v}(x, z)\, dz\, dx + \int\limits_w^e \int\limits_{\underline{\overline{z}_\sigma(\sigma) + z'_\sigma(\sigma)}\,\overline{z}_\sigma(\sigma) + z'_\sigma(\sigma, t)}^{\underline{z_\sigma(0)}\,\eta} v'(x, z, t)\, dz\, dx \tag{19}$$

$$\begin{aligned}
= \underbrace{\int\limits_w^e \int\limits_{\overline{z}_\sigma(\sigma)}^{\eta} \overline{v}\, dz\, dx}_{\text{mean}} + \underbrace{\int\limits_w^e \int\limits_{\overline{z}_\sigma(\sigma) + z'_\sigma(\sigma, t)}^{\overline{z}_\sigma(\sigma)} \overline{v}\, dz\, dx}_{\text{density variation}} \\
+ \underbrace{\int\limits_w^e \int\limits_{\overline{z}_\sigma(\sigma)}^{\eta} v'\, dz\, dx}_{\text{velocity variation}} + \underbrace{\int\limits_w^e \int\limits_{\overline{z}_\sigma(\sigma) + z'_\sigma(\sigma, t)}^{\overline{z}_\sigma(\sigma)} v'\, dz\, dx}_{\text{density}-\text{velocity covariation}}
\end{aligned} \tag{20}$$

~~where the first and third terms on the RHS are integrals between the mean depth of the σ isopycnal and the surface, and the second and fourth terms integrate between the instantaneous and mean depths of the σ isopycnal. We write this more concisely as~~

where the first two terms on the RHS integrate the time-mean velocity field and the last two the velocity anomalies. The first and third terms on the RHS are integrals between the depth of the time-mean σ isopycnal and the surface, and the second and fourth terms integrate between the instantaneous and time-mean isopycnal depths. We write this more concisely as

$$\Psi_\sigma(\sigma, t) = \Psi_{\overline{\sigma}\,\overline{v}}(\sigma) + \Psi_{\sigma'\,\overline{v}}(\sigma, t) + \Psi_{\overline{\sigma}\,v'}(\sigma, t) + \Psi_{\sigma'\,v'}(\sigma, t) \tag{21}$$

Removing the long-term mean ($\overline{\Psi_\sigma}$) from all terms and taking monthly means to examine the seasonal cycle leaves:

$$\Psi'_\sigma(\sigma,m) = \Psi'_{\sigma'\overline{v}}(\sigma,m) + \Psi'_{\overline{\sigma}v'}(\sigma,m) + \Psi'_{\sigma'v'}(\sigma,m) \tag{22}$$

where m now indicates these are mean monthly anomalies from the long-term mean.

210

We further decompose the velocity anomaly into a surface Ekman driven component, $v'_{Ek}(x,z,t)$ (calculated from the wind stress, with uniform compensating flow below the surface layer), and a remainder, $v''(x,t)$.

$$\Psi'_{\overline{\sigma}v'}(\sigma,m) = \Psi'_{\overline{\sigma}v'_{Ek}}(\sigma,m) + \Psi'_{\overline{\sigma}v''}(\sigma,m) \tag{23}$$

215   The density anomaly is decomposed in two ways, applied independently. Firstly, into a part due to temperature anomalies (with salinity held at the long-term mean) σ'_T, a part due to salinity anomalies (with temperature held at the long-term mean) σ'_S, and a part σ'_{TS} due to the non-linearities in the equation of state.

$$\Psi'_{\sigma'\overline{v}}(\sigma,m) \approx \Psi'_{\sigma'_T\overline{v}}(\sigma,m) + \Psi'_{\sigma'_S\overline{v}}(\sigma,m) + \Psi'_{\sigma'_{TS}\overline{v}}(\sigma,m). \tag{24}$$

This equality is approximate because of the non-linearities in the velocity and density fields.

220   Secondly, we decompose the density anomaly into a part due to zonally uniform density anomalies $\langle\sigma'\rangle$ and a remainder σ''.

$$\Psi'_{\sigma'\overline{v}}(\sigma,m) \approx \Psi'_{\langle\sigma'\rangle\overline{v}}(\sigma,m) + \Psi'_{\sigma''\overline{v}}(\sigma,m). \tag{25}$$

The zonally uniform seasonal density anomaly term, $\langle\sigma'\rangle$, has little signal below $500\,\mathrm{m}$. This decomposition was chosen in part because the zonally uniform density anomaly term has no spatial density gradients and is therefore independent of the geostrophic velocity field.

225   Finally, note that since MOC_σ and σ_{MOC} are functions of the maximum of the streamfunction Ψ_σ, we cannot calculate their anomalies directly from the anomalies in Eqs. 22 to 25. We must first add back in the long-term mean ($\overline{\Psi_\sigma}$) and then calculate the MOC_σ anomalies. For example, for the total anomaly:

$$\mathrm{MOC}'_\sigma(\Psi'_\sigma) = \mathrm{MOC}_\sigma(\Psi'_\sigma + \overline{\Psi_\sigma}) - \mathrm{MOC}_\sigma(\overline{\Psi_\sigma}) \tag{26}$$

We have described the decomposition in density space, but Eqs. 16 to 26 have exact parallels in temperature and salinity
230 space which we will not detail here.

3 Results

We present the characteristics of the seasonal cycle at OSNAP obtained by applying the above density-space analysis to the 20-year model output. First we consider the full OSNAP section (Sect. 3.1.1), before separately examining OSNAP_E and OSNAP_W (Sect. 3.1.2), then we use the model results to aid interpretation of OSNAP observations (Sect. 3.2) and finally we look at heat and freshwater fluxes (Sect. 3.3).

The modelled mean overturning streamfunction in density space for the full OSNAP line ($\overline{\Psi_\sigma}$, Fig. 2g) shows the well-known, classic shape, with net northward flow at lower densities and net southward flow at higher densities. The modelled MOC_σ of the mean overturning, $(\max(\overline{\Psi_\sigma}))$ is about $13\,\text{Sv}$ and occurs at density $\sigma_{\text{MOC}} = 27.55$. These values are both lower than found in the observational data (Fig. 3g), but the structure of the modelled streamfunctions is close enough to the observations to give confidence in the modelled overturning.

3.1 Modelled seasonal cycles

3.1.1 Full OSNAP section

~~The monthly overturning streamfunction anomalies ($\Psi'_\sigma(\sigma,m)$,~~ In these results we will rely on several figures with a form similar to Fig. 4~~,~~ so it is worth spending some time here familiarising ourselves with the format and the interpretation. The top row of panels (a-e) all have density on the y-axis. Panel (a) ~~have a dominant dipole structure in both density and time. At lower densities (less than about 27.4) positive overturning streamfunctionanomalies peak in the autumn with negative anomalies peaking in spring. Conversely, at higher densities(greater than 27.4) positive streamfunction anomalies peak in the spring with negative anomalies peaking in autumn. The density of maximum overturning also varies through the year, as might be expected, with a maximum in spring when watersare densest after winter cooling, and minimum in autumn. Note that the density of maximum overturning does not coincide with the density where the largest streamfunction anomalies are found, so the seasonal cycle in MOC_σ~~ Fig. 4f, which approximately samples the anomalies at density σ_{MOC} (green line in Fig. 4b) is simply the mean overturning streamfunction~~, mostly samples the higher densities but misses the extremes of the seasonal cycle at both higher and lower densities. The density flux (Fig. 4j), the integral in density of the overturning streamfunction anomalies, shows maximum southward density flux (largest negative values) in June and minimum in January, lagging 2 to 3 behind the meridional overturning seasonal signal.~~ transport accumulated from low to high densities, in density space. Panels (b-e) are Hovmöller plots of seasonal streamfunction anomalies with months on the x-axis. In these plots blue areas correspond to densities with reduced northward flow at lower densities compared to the mean, and red areas to densities with increased northward flow of lighter waters. Panels (c) and (d) decompose the total anomalies in (b) into components due to density variability combined with the mean flow (c), and flow variability combined with the mean densities (d). In the density-variability plots, blue areas signify either increased density of northward flows or reduced density of southward flows. And vice-versa for red areas.

If we consider for example March in Fig. 4c, we see negative anomalies at densities peaking at $27.2\,\text{kg m}^{-3}$. Looking at Fig. 5a, the $27.2\,\text{kg m}^{-3}$ isopycnal is only present in the eastern basin; and Fig. 5b,c shows the density anomalies to be
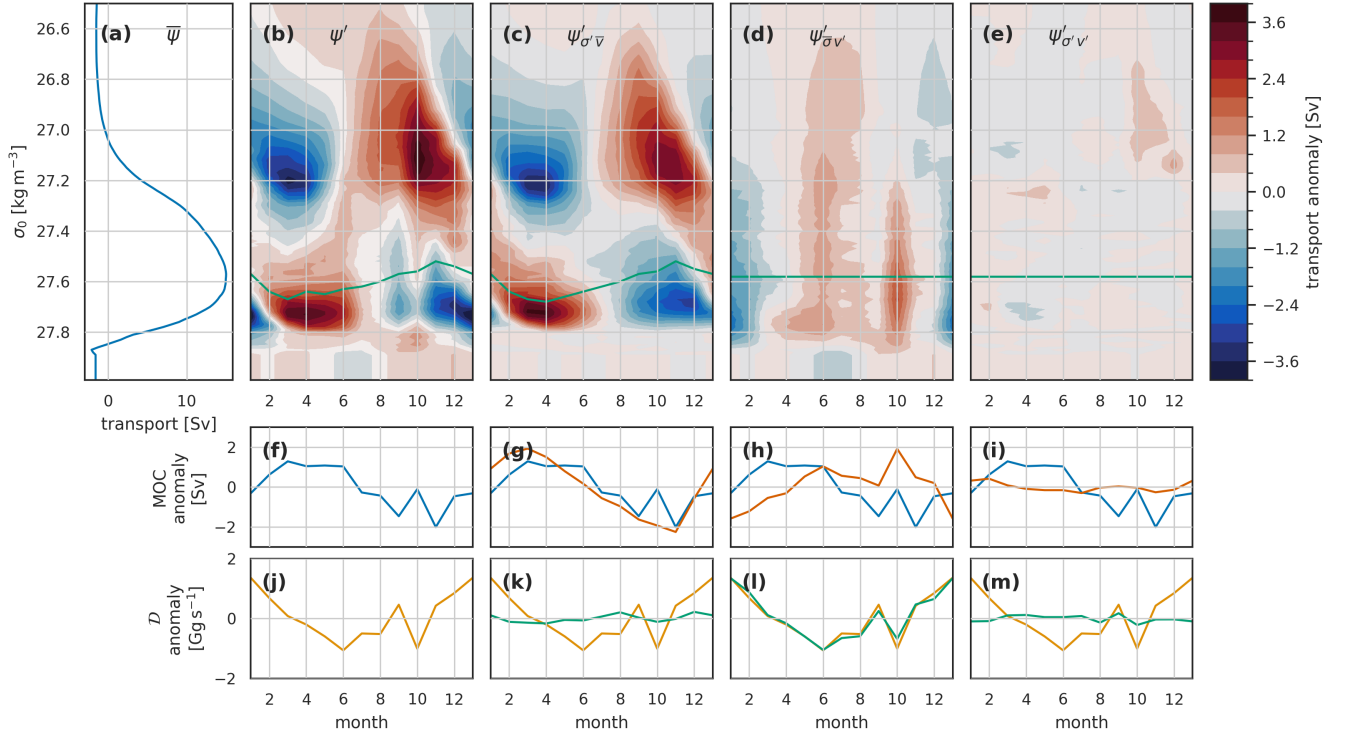
Figure 4. The seasonal cycle in the overturning streamfunction (Ψ), MOC and density flux ($\mathcal{D}$) for the full OSNAP transect in the Viking20x model. (a) the mean overturning streamfunction. (b-e) Hovmöller (time – σ) plots of seasonal streamfunction anomalies. The green line in each shows the associated variability of σ_{MOC}. The plots are arranged in columns: (b,f,j) the full anomalies, (c,g,k) the anomalies associated with density variations and mean velocities, (d,h,l) velocity variations and mean density, (e,i,m) velocity and density co-variation. The lower two rows are MOC (f-i) and density flux $\mathcal{D}$ (j-m). In (g-i) the blue line is for the total anomalies, copied across from panel (f), while the orange line is the respective anomaly component. Similarly, the yellow, total anomaly line in (j) is repeated in panels (k-m) alongside the green line showing the respective components of density flux anomaly.

confined to the near-surface. So the negative March streamfunction anomaly is the result of winter cooling in the predominantly

265 northward-flowing surface waters. We find very little, if any, lighter-than-average waters in March, so the positive anomaly between $27.5\,\mathrm{kg\,m^{-3}}$ and $27.8\,\mathrm{kg\,m^{-3}}$ must be due to denser-than-average southward flowing water. Southward flowing waters in this density range are found in the East Greenland and Labrador Sea currents Fig. 5a. For the full OSNAP section the East Greenland Current anomalies largely cancel with the northward flow just downstream in the West Greenland Current, so the positive March, density-driven streamfunction anomalies (Fig. 4c) are largely due to seasonal denser waters flowing south in

270 the Labrador Current.

The velocity-driven anomalies, Fig. 4d, are perhaps simpler to understand. Positive anomalies, such as those observed in June, result from stronger than average northward flow (or weaker than average southward flow) of light water which must be combined with stronger than average southward flow (weaker northward) of dense water. Lighter waters are generally found at
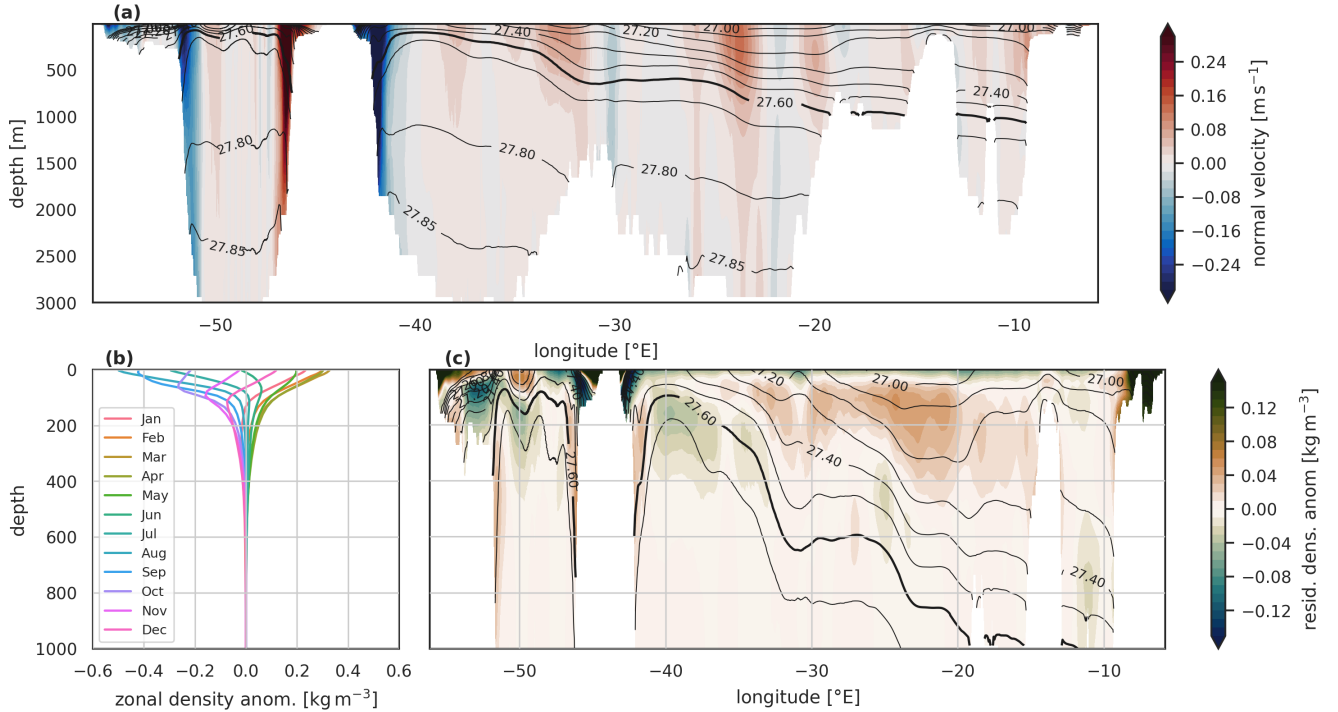
Figure 5. Panel (a): shading shows the long-term mean northward velocity normal to the OSNAP section in the Viking20x model, the long-term mean potential density contours are overlaid. The $\sigma_0 = 27.6$, the approximate mean σ_{MOC}, contour is highlighted. The strong boundary currents in the west are clearly seen, as is the deepening of the density contours towards the east. Panel (b): seasonal cycle of model zonal-mean monthly density anomalies. Note that the zonal mean seasonal density variability is largely confined to the surface 200 m, and almost entirely confined to the surface 500 m. The maximum positive seasonal anomalies (densest surface waters) are found in March-April at all depths, the maximum negative anomalies (lightest waters) are found between August and December depending on depth. The deeper layers lag the surface layers in seasonal minimum densities. Panel(c), shading shows the remainder density anomalies, after the zonal mean anomalies are removed, for **March**, when surface waters are at their densest. Notice the smaller amplitude of these remainders compared to the zonal mean anomalies. The zonal mean March anomalies would take the form of strogly positive anomalies on this plot, so red colours here are areas where the zonal mean underestimates the spring density maximum, and green colours where the zonal mean is an overestimate.

the surface or in the east. So positive velocity-driven anomalies could due to: stronger northward (weaker southward) surface velocities balanced by adjustment of return flow at depth; or stronger, more barotropic, flow north in the east and south in the west, for example an increased subpolar gyre. The final plot on the top line Fig. 4e, is residual anomalies associated with covariation of density and velocity and is always small.

The remaining line on Fig. 4b-d, the green line, shows the monthly evolution of σ_{MOC}. The streamfunction anomaly along this line is (very nearly) the MOC anomaly plotted below in Fig. 4(f-i). From the position of this line in density space,

relative to the streamfunction anomalies, we see that the total and density-driven seasonal MOC variability is largely driven by the variability at higher-densities, that is by the seasonal density variation, near-surface, in the southward-flowing Labrador Current. The velocity variability drives little change in σ_{MOC}.

The final row of panels, Fig. 4j-m, show the density flux, which is the minus one times the integral in density of the anomalies, i.e. the integral from top to bottom of the panels (b-e). Here we see that when integrated, the dipole structure which dominates the density-driven anomalies results in very little density flux - that is while the shape of the streamfunction curve changes seasonally with density variability, the area beneath remains fairly constant. In contrast, the velocity variability dominates the density flux since, although the associated anomalies are small compared to the density-driven, they maintain consistent sign across the full density range.

Using the above guidance to interpret Fig. 4 we see that the monthly overturning streamfunction anomalies ($\Psi'_\sigma(\sigma, m)$, Fig. 4b) have a dominant dipole structure in both density and time. At lower densities (less than about $27.4 \, \mathrm{kg \, m^{-3}}$) positive overturning streamfunction anomalies peak in the autumn with negative anomalies peaking in spring. Conversely, at higher densities (greater than $27.4 \, \mathrm{kg \, m^{-3}}$) positive streamfunction anomalies peak in the spring with negative anomalies peaking in autumn. While the density of maximum overturning also varies through the year, with a maximum in spring when waters are densest after winter cooling, and minimum in autumn, it always lies within the higher density range. So the seasonal cycle in MOC_σ Fig. 4f, which approximately samples the anomalies at density σ_{MOC} (green line in Fig. 4b), samples the higher densities resulting in the sping maximum and autumn minimum in MOC_σ. The density flux (Fig. 4j), shows maximum southward density flux (largest negative values) in June and minimum in January, lagging 2 to 3 months behind the meridional overturning seasonal signal.

We now decompose the overturning streamfunction anomalies into separate parts driven by seasonality in density and velocity (Eq. 22, Fig. 4c-e). The dipole structure occurs in the anomalies associated with density variability ($\Psi'_{\sigma' \overline{v}}(\sigma, m)$, Fig. 4c). The seasonal cycle at lighter densities, with its peak in autumn, is caused by the seasonal cycle in density of northward flowing water. The cycle is reversed for denser waters, with peak positive overturning streamfunction anomalies in spring, ~~because denser waters flow~~ we discussed above how this is due to these denser surface waters flowing predominantly southward. The seasonal velocity variability drives a different pattern of overturning streamfunction variability, with consistent sign across almost the whole density range ($\Psi'_{\overline{\sigma} v'}(\sigma, m)$, Fig. 4d). This annual cycle has its minimum in January and peaks in July, with a secondary, sharp, peak in October. This pattern corresponds with an increase in net ~~inflow~~ northward flow of lighter waters in phase with a net ~~outflow~~ southward flow of denser waters. ~~The streamfunction variability associated with co-variance of velocity and density is everywhere small ($\Psi'_{\sigma' v'}(\sigma, m)$, Fig. 4e).~~

The resulting seasonal variability in the meridional overturning (Fig. 4f-i) is mostly due to the seasonal density variation (Fig. 4g), and in particular the seasonal density variation of denser waters. The velocity variation acts mostly to delay the MOC seasonal peak and introduce some higher-frequency variability in the autumn. In contrast, the seasonal northward density flux anomalies (Fig. 4j-m) are almost entirely due to the velocity variability (Fig. 4l).

Decomposing the overturning streamfunction further, beginning with the velocity-driven component (Fig. 6), we find the dominant factor to be the seasonal cycle in surface Ekman transport. This produces seasonal overturning streanmfunction

315 variability with a maximum in summer minimum in winter. The timing is due to the surface Ekman transport being generally southward, opposing the overturning. The summer maximum corresponds to a minimum in this opposition. The streamfunction variability shows as a summer ~~MOC~~ MOC maximum and northward density flux minimum (i.e. southward maximum). The remainder again shows a narrow peak overturning streamfunction anomaly in the autumn, we have been unable to discover the precise cause of this but it appears to be located in the barotropic transport variability. The shorter, 6-year, model results

320 show a stronger seasonal cycle driven by the barotropic velocity variability (Fig. S1c) suggesting interannual variability of the seasonal cycle.

Turning to the density-driven component, we decompose this in two independent and complementary ways. First separating out the component associated with zonal mean seasonal cycle of density, and secondly into two components due to temperature and salinity variations. The zonal mean seasonal cycle of density is almost entirely confined to the surface $500\,\mathrm{m}$ (Fig. 5), and

325 accounts for almost all the density-driven variability in MOC and most of that in the overturning streamfunction (Fig. 7). The domination of the zonal mean density signal in MOC variability is due to the seasonal cycle of summer/autumn lighter surface densities and winter/spring denser surface waters in the near-surface southward flow. This southward flow occurs primarily in the East Greenland Current and Labrador Current. Because much of the East Greenland Current flows back northwards as the West Greenland Current much of that transport cancels, leaving the OSNAP-wide seasonal MOC variability largely dominated

330 by near-surface density changes in the Labrador Current.

~~Further exploration of the~~ The variability in the density-driven streamfunction remainder (Fig. 7d) ~~shows the lower-density remainder (centred at 27.2)to be due to~~ has the same pattern as that associated with the seasonal zonal mean density variation (Fig. 7c), but lower amplitude, suggesting that the zonal mean ~~underestimating seasonal mixed layer depth and density variability in the North Atlantic Current in the east of the section. The remainder at higher densities (centred at 27.7~~ annual

335 density signal is underestimating the annual signal in both lighter northward flows ($\sigma < 27.4\,\mathrm{kg\,m^{-3}}$) ~~is similarly due to underestimation of the seasonal cycle of isopycnal depth in the Labrador Current outflow~~ and denser ($\sigma > 27.6\,\mathrm{kg\,m^{-3}}$) southward flows. Figure 5c confirms this, with dense anomalies present in March in the widespread near-surface northward flow (15-30°W, surface 200-400 m) and also in the strong southward flow below 300 m on the Labrador coast. These remainders have ~~no~~ little expression in the MOC because of the density at which they occur. The two effects largely cancel in the

340 density flux metric~~, this~~. This cancellation appears to be by chance ~~and not true~~ for the full OSNAP section, and does not hold for the separate OSNAP$_\mathrm{E}$ and OSNAP$_\mathrm{W}$ calculations below. Note that the isopycnal depth change in the Labrador Current outflow is the only notable seasonal influence we see on the overturning streamfunction in the model from below 500 m, here down to $800-1000\,\mathrm{m}$, some seasonal deep density variation in the Rockal Trough can be seen but it is in a region of low velocity so does not impart the overturning streamfunction.

345 Finally we examine the separate contributions of seasonal temperature and salinity variability to the density-driven seasonal cycle (Fig. 8). The seasonal cycle in the overturning streamfunction is dominated by temperature variability, ~~with the~~ responsible for the dipole pattern in both density and time. The influence of salinity variability is mostly confined to the upper limb where ~~it generally opposes the temperature variability~~ $\sigma < 27.6\,\mathrm{kg\,m^{-3}}$ (Fig. 8b-d). While the seasonal cycle in the overturning streamfunction seasonal variability is dominated by temperature~~variability~~, both MOC and density flux seasonal
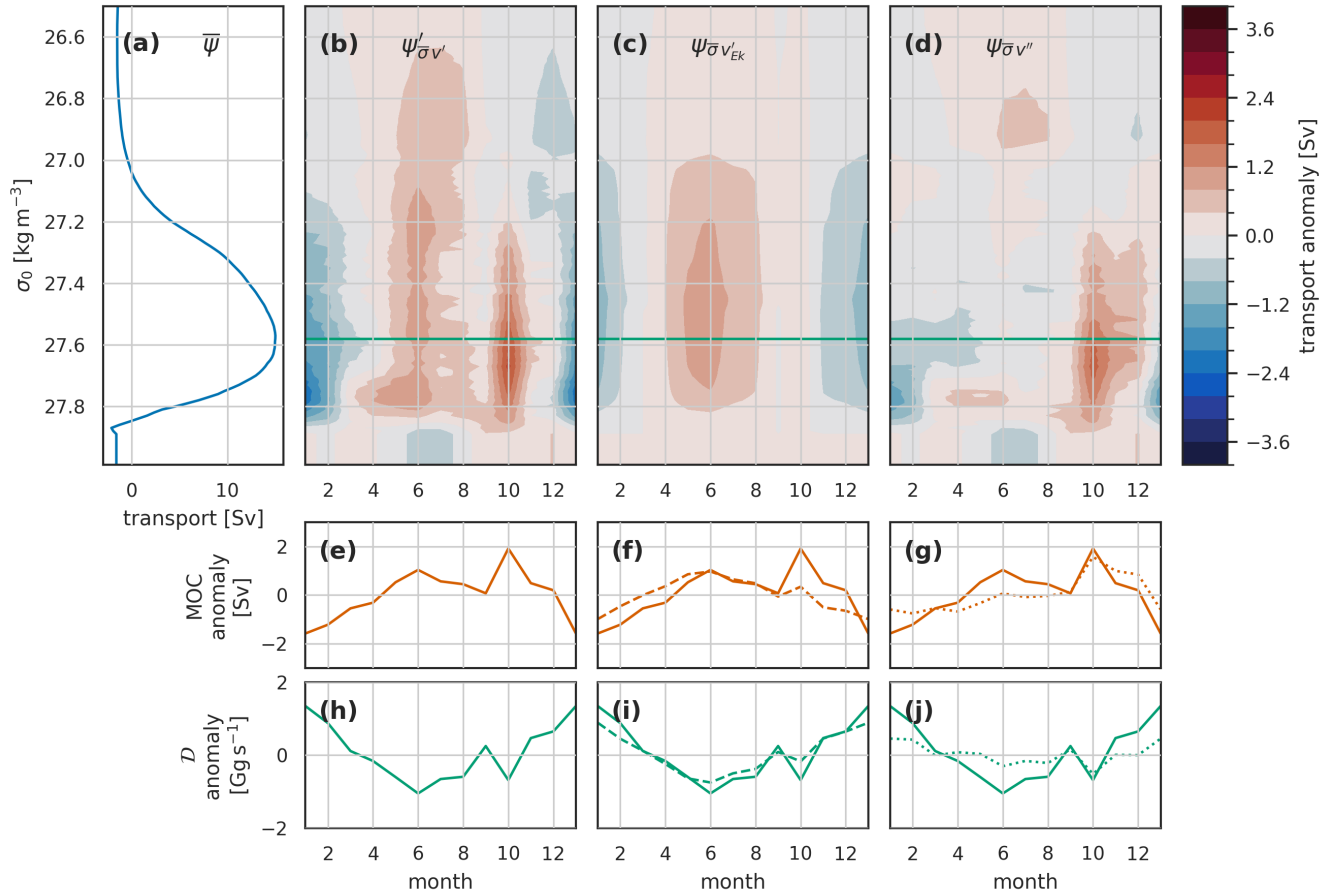
Figure 6. The seasonal cycle due to velocity variability (constant mean density structure) in the overturning streamfunction (Ψ), MOC and density flux ($\mathcal{D}$) for the full OSNAP transect in the Viking20x model. (a) the mean overturning streamfunction. (b-d) Hovmöller (time – σ) plots of seasonal streamfunction anomalies. The green line in each shows the associated variability of σ_{MOC}. The plots are arranged in columns: (b,e,h) the full velocity-driven anomalies, (c,f,i) velocity-driven anomalies associated with Ekman surface velocity variability, and (d,g,j) the anomalies associated with the remainder of the velocity variability. The lower two rows are MOC (e-g) and density flux $\mathcal{D}$ (h-j). In (f,g) the solid orange line is for the total velocity-driven MOC anomalies, copied across from panel (e); the dashed line in (f) is the Ekman driven MOC anomaly; and the dotted line in (g) is the remainder-driven MOC anomaly. Similarly, the solid green total density flux anomaly line in (h) is repeated in panels (i,j) alongside the dashed line in (i) showing the Ekman driven $\mathcal{D}$ and the dotted line in (j) is the remainder-driven $\mathcal{D}$ anomaly.

350 cycles have fairly equal ~~amplitude~~ contributions from temperature and ~~salinty variability . This is bacause sampling~~ salinity variability (Fig. 8f,g,i,j). MOC, sampling the streamfunction at the maximum ~~of the streamfunction for MOC~~ (green line in (Fig. 8b-d) does not capture the maximum temperature-driven ~~anomalies~~anomaly, and integrating the anomalies in density space for the density flux involves cancellation of the large positive and negative temperature-driven anomalies (Fig. 8c,f,i).

Figure 7. Similar to Fig. 6 but for the seasonal cycle due to density variability (constant mean velocity structure) in the overturning streamfunction (Ψ), MOC and density flux ($\mathcal{D}$) for the full OSNAP transect in the Viking20x model. This figure has the same structure as Fig. 6 but the columns here refer to: (b,e,h) the full density-driven anomalies, (c,f,i) density-driven anomalies associated with zonal mean density variability, and (d,g,j) the anomalies associated with the remainder of the density variability.

The overall smaller amplitude salinity-driven streamfunction anomalies however, with a simpler single peaked form in density, are more efficiently expressed in both MOC – where the streamfunction anomaly occurs at densities including σ_{MOC} – and density flux –since there is no cancellation of anomalies when integrating in density space (Fig. 8d,g,j).

The opposition between Interestingly, while temperature and salinity anomalies at lower densities is seen in the density flux anomalies (Fig. 8h-j) where temperature and salinity contributions to the density fluxlargely cancel producing no net

contributions to MOC are in phase – both with a spring maximum and autumn minimum – the contributions to density flux are out of phase – temperature variability producing a spring maximum in northward density flux (minimum southward) while salinity variability shows a spring maximum southward density flux. Naively, we might expect both stronger MOC and more southward density flux when overturning is larger, this is what we observed in the velocity-driven component described above and in the salinity-driven component here. In the temperature-driven component the phase relationship between density flux and MOC is reversed. As for the total density-driven MOC above, the temperature-driven seasonal MOC is dominated by the southward-flowing water in the western boundaries, whereas the density flux seasonality dominated by the larger streamfunction variability at lower densities associated with northward surface flow in the eastern basin.

The salinity-driven streamfunction cycle (Fig. 8d) appears to be the result of two regional seasonal cycles in surface salinity. There is slight winter freshening due to excess precipitation over evaporation across the interior and east of the basin. This tends to reduce density, in opposition to cooling increasing density, and results in the largely opposite phase of salinity- and temperature-driven streamfunction variability at where $\sigma < 27.4\,\mathrm{kg\,m^{-3}}$. At the western boundaries, particularly in the shallow shelf regions, salinity minimum occurs in late summer due to freshwater input from ice melt. These coastal waters are still part of the upper limb but flowing southward, so this autumn salinity and density minimum produces negative streamfunction anomalies. We look at this in more detail when discussing OSNAP$_\mathrm{E}$ and OSNAP$_\mathrm{W}$ separately, below.

To aid comparison with the seasonal cycles of MOC and density flux for OSNAP$_\mathrm{E}$ and OSNAP$_\mathrm{W}$ and in the OSNAP observational data we bring together the MOC and density flux plots from Figs. 6, 7 and 8 in Fig. 9.

3.1.2 OSNAP East and OSNAP West

Due to constraints of space we do not show the full streamfunction anomalies individually for OSNAP$_\mathrm{E}$ and OSNAP$_\mathrm{W}$. However, the fundamental structure of the anomalies is the same for the part-sections as for the full section: the overall anomalies being dominated by the dipole structure in seasonal density-driven anomalies, while the velocity-driven anomalies have a simpler seasonal cycle with coherent sign across the full density range. The main differences between OSNAP$_\mathrm{E}$ and OSNAP$_\mathrm{W}$ streamfunction anomalies is in the densities where the maxima and minima are positioned. At OSNAP$_\mathrm{E}$ the lower-density anomalies, associated with northward flow, are much as for the full section. The higher-density anomalies, associated with southward flow, now in crossing OSNAP$_\mathrm{E}$ in the East Greenland current, occur at lower densities than for the higher-density anomalies in full section which we attributed to the Labrador Current. This reflects the further densification of waters within the Labrador Sea. For OSNAP$_\mathrm{W}$, the anomalies at lighter densities associated with northward flow closely mirror the dense OSNAP$_\mathrm{E}$ southward flow anomalies. Supporting the idea of notable 'cancellation' of East and West Greenland
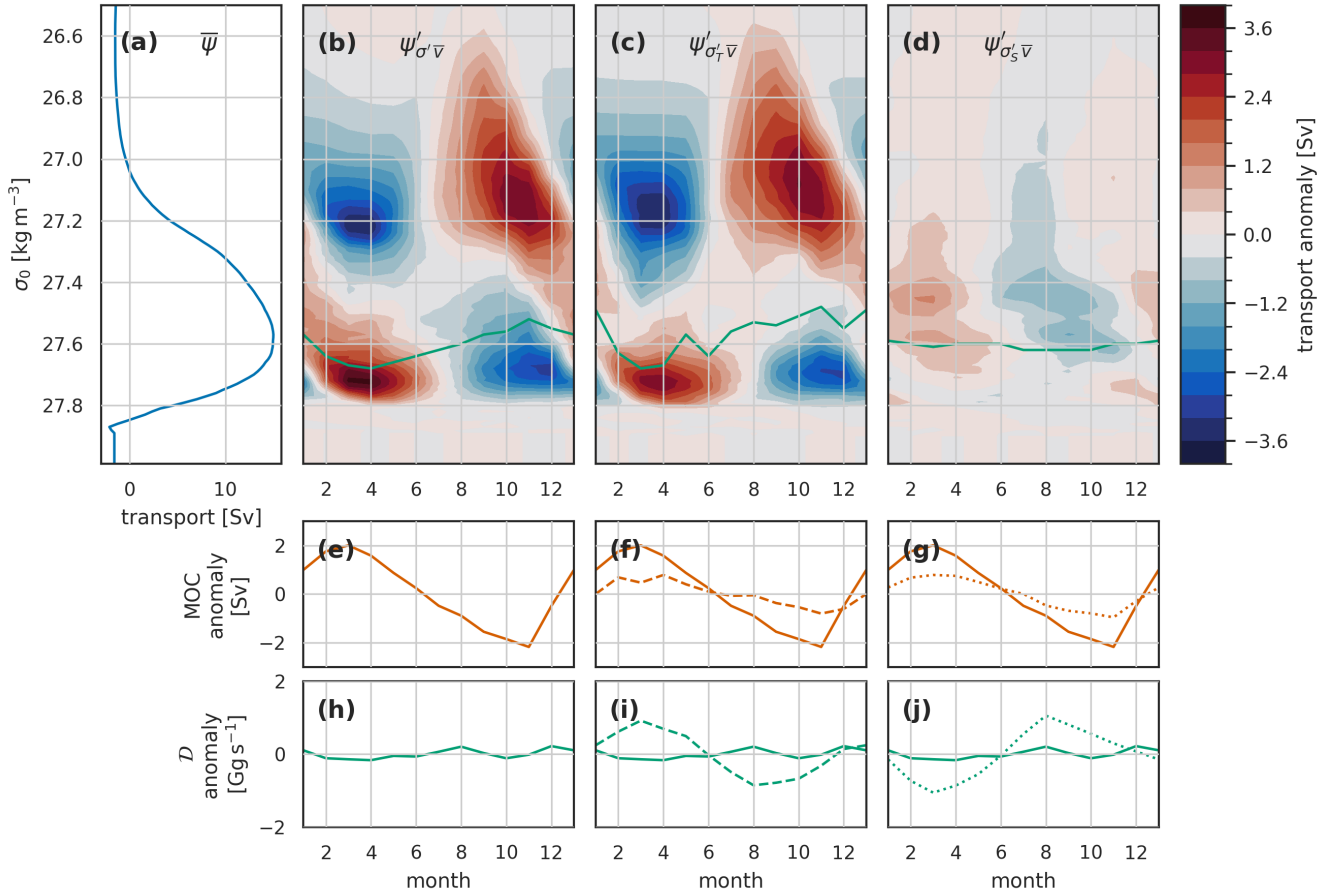
Figure 8. Similar to Fig. 7 but for the decomposition of the seasonal cycle due to density variability into separate components driven by temperature and salinity variability. This figure has the same structure as Fig. 7 but the columns here refer to: (b,e,h) the full density-driven anomalies, (c,f,i) density-driven anomalies associated with temperature variability, and (d,g,j) the anomalies associated with salinity variability.

Currents when the full section is considered. The denser OSNAP$_W$ anomalies closely resemble the dense anomalies in the full section.

The resulting seasonal cycles of MOC and density flux on the individual OSNAP$_E$ (Fig. 10) and OSNAP$_W$ (Fig. 11) sections bear many similarities to the full section (Fig. 9). In all cases the seasonal cycle of the overturning circulation, MOC, is dominated by the component due to density variation, and specifically by the seasonal cycle of density in the southward surface flow at the western boundary. The Ekman contribution is largely confined to OSNAP$_E$, this is ~~as expected~~ due to the orientation of the prevailing wind vectors eastward along OSNAP$_E$ (driving surface flow southward across the section) but across OSNAP$_W$ driving along-section flow which does not contribute to overturning).
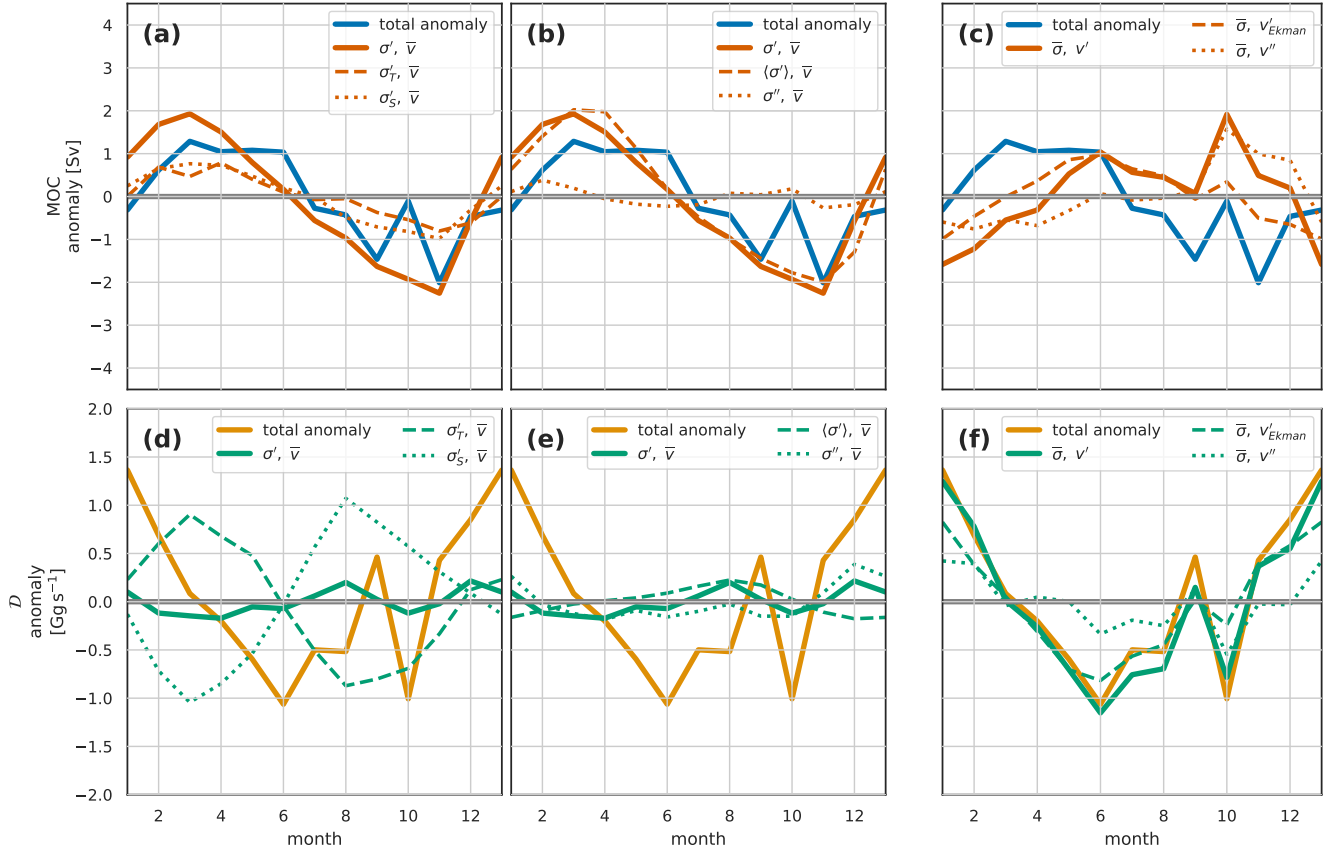
Figure 9. Summary plot of the decomposition of the seasonal cycle for the **full OSNAP section** of (a-c) MOC_σ and (d-f) density flux $\mathcal{D}$ for the **Viking20x model**. The left-hand column (a,d) shows the density-driven decomposition into temperature and salinity components; the middle column the density-driven decomposition into zonal mean and remainder; and the right-hand column the velocity-driven decomposition into Ekman and remainder components. The blue line repeated in (a-c) is the total MOC_σ anomaly; the solid orange line is either the total density-driven anomaly component of MOC_σ (a,b), or the total velocity-driven component (c). The dashed and dotted lines in (a-c) are respectively: in (a) the temperature and salinity driven components; in (b) the zonal mean density and density-driven remainder components; and in (c) the Ekman driven and velocity-driven remainder components. Similarly, for (d-f) the repeated yellow line is the total $\mathcal{D}$ anomaly; the solid green line is either the total density-driven anomaly component of $\mathcal{D}$ (d,e), or the total velocity-driven component (f). The dashed and dotted lines in (d-f) are respectively: in (d) the temperature and salinity driven components; in (e) the zonal mean density and density-driven remainder components; and in (f) the Ekman driven and velocity-driven remainder components. Several of the figures following share this format so it is worth spending a moment to understand it.

Perhaps the most notable difference between the full OSNAP section and both OSNAP_E and OSNAP_W is that while the density-driven seasonal density flux anomalies across OSNAP ~~was~~ were small (Fig. 9d,e) they are a significant factor in the seasonal cycles at both OSNAP_E and OSNAP_W. The OSNAP_E and OSNAP_W density fluxes cancel when considering the full
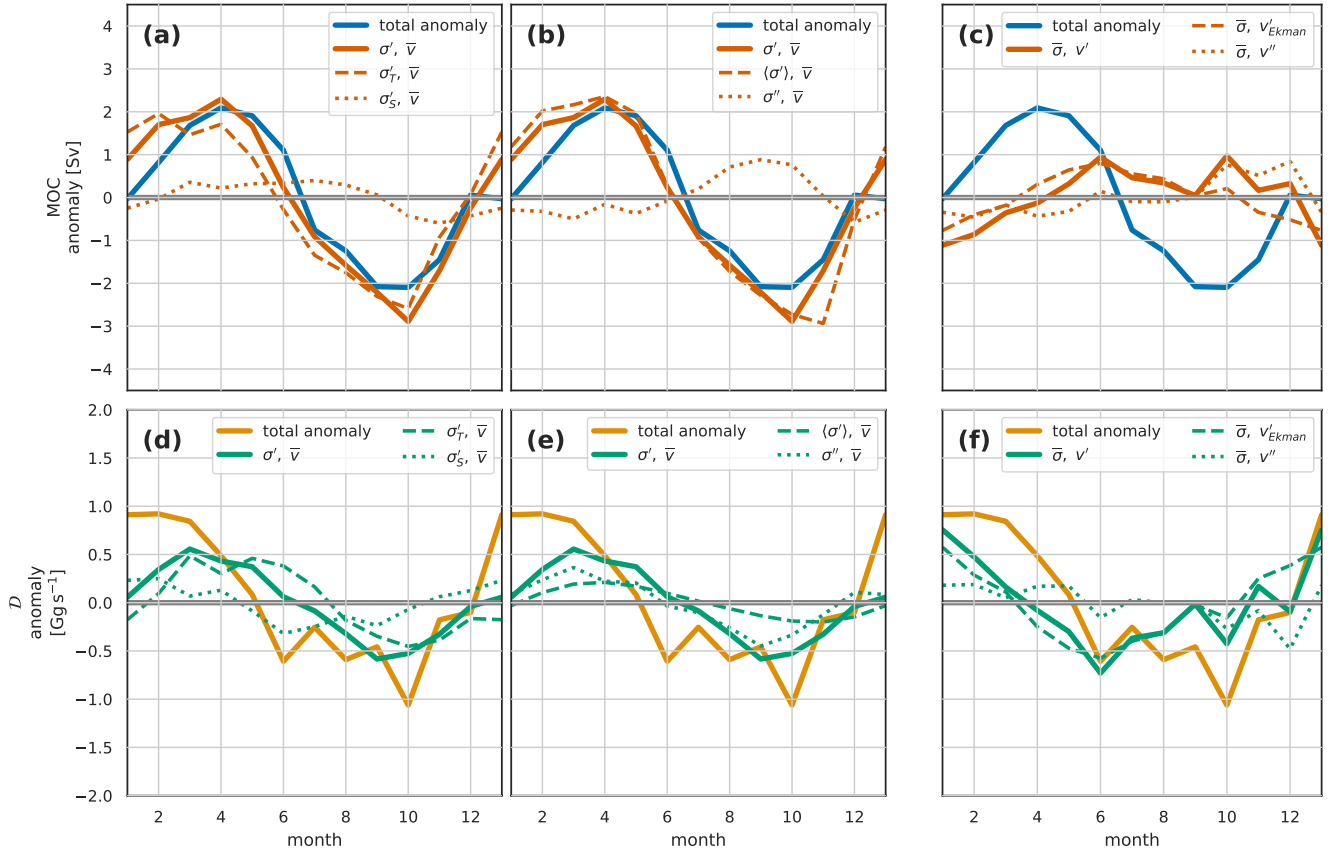
Figure 10. As for Fig 9 but for the **Viking20x model** seasonal cycle at **OSNAP$_E$**.

section. This cancellation is largely explained by variability associated with the East Greenland Current flowing southward across OSNAP$_E$ being strongly correlated with that of the West Greenland Current flowing northward across OSNAP$_W$.

~~Compared~~ OSNAP$_E$, compared to the full OSNAP section (Fig. 9), ~~OSNAP$_E$~~ shows more domination of both MOC and density flux seasonal cycles by temperature variability (Fig. 10a,d), with the salinity component confined almost entirely to OSNAP$_W$. OSNAP$_E$ seasonal temperature variability is also the source of the slightly ~~counterintuitive~~ counter-intuitive result where enhanced MOC is associated with weaker southward density flux.

~~As~~ For OSNAP$_W$, as for the full section, ~~in OSNAP$_W$~~ temperature- and salinity-driven seasonal variability reinforce each other for MOC but are opposed for density flux (Fig. 10a,d). ~~The salinity signal here dominating the density-driven~~ OSNAP$_W$ is the only region where the salinity signal dominates, at least for the density flux. The ~~density-driven density flux in turn dominates the total density flux at OSNAP~~ timing of the salinity-driven density-flux cycle, its domination by OSNAP$_W$, the density of the associated largest streamfunction anomalies (Fig 8), and the domination of all the seasonal cycles by near-surface
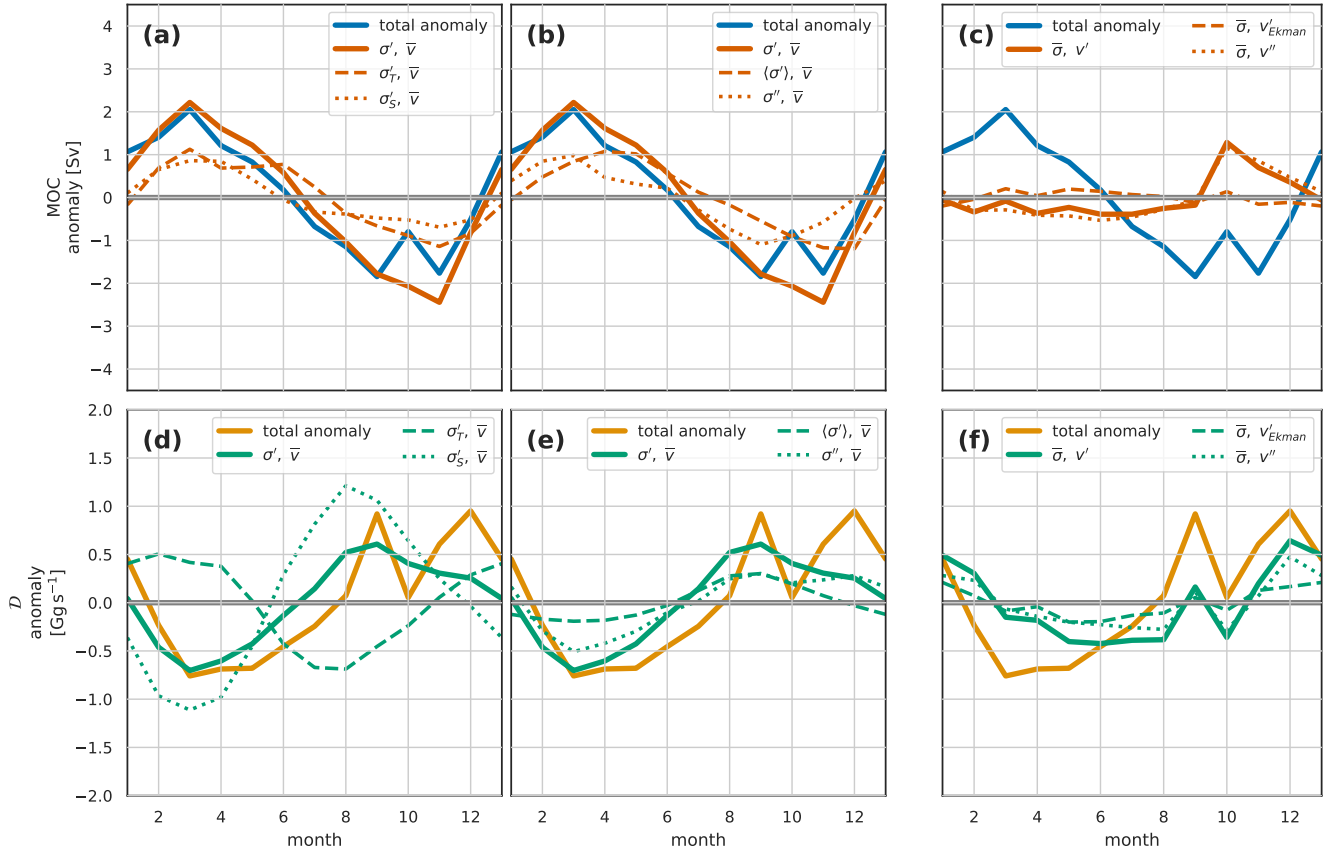
Figure 11. As for Fig 9 but for the **Viking20x model** seasonal cycle at **OSNAP$_W$**

variability, point to the salinity-driven part of the seasonal cycle of overturning at OSNAP being largely driven by the seasonal cycle of salinity in the shallow coastal part of the Labrador Current.

In the full section, the decomposition of density-driven variability into zonal-averaged seasonal cycle and a remainder (Fig. 7) ~~neatly resulted in no residual contribution~~ produced no net contribution from the remainder to either MOC or density flux, though ~~some variability is~~ variability was seen in the residual streamfunction (Fig. 7d). ~~This~~ We showed (Fig. 5) that this residual streamfunction variability is made of two spatially separate contributions: the contribution at lighter densities is due to the ~~zonal mean seasonal cycle underestimating the seasonal cycle~~ seasonal cycle in the North Atlantic Current in the eastern part of OSNAP$_E$; while the contribution at higher densities is due to the ~~zonal mean underestimating the~~ seasonal cycle of ~~isopycnal heave~~ density deeper in the Labrador current outflow across OSNAP$_W$. ~~This residual contribution is the key factor~~ The contribution from the remainder term to the density-driven density flux is now split between OSNAP$_E$ and OSNAP$_W$, resulting in the larger, opposing, contribution of density-driven anomalies to the seasonal cycle of density flux in ~~both~~ OSNAP$_E$ and OSNAP$_W$ when compared to the full OSNAP section.

It should be noted that while the density fluxes in OSNAP$_\mathrm{E}$ and OSNAP$_\mathrm{W}$ sum to the full OSNAP density fluxes the same does not hold for MOC as σ_MOC is significantly denser in OSNAP$_\mathrm{W}$ than OSNAP$_\mathrm{E}$.

3.2 Observed seasonal cycles

3.2.1 Full OSNAP section

The mean seasonal cycle of the overturning streamfunction (Fig. 12a) in the observations is very similar to the model (Fig. 4a) though with the peak overturning at a slightly higher density.
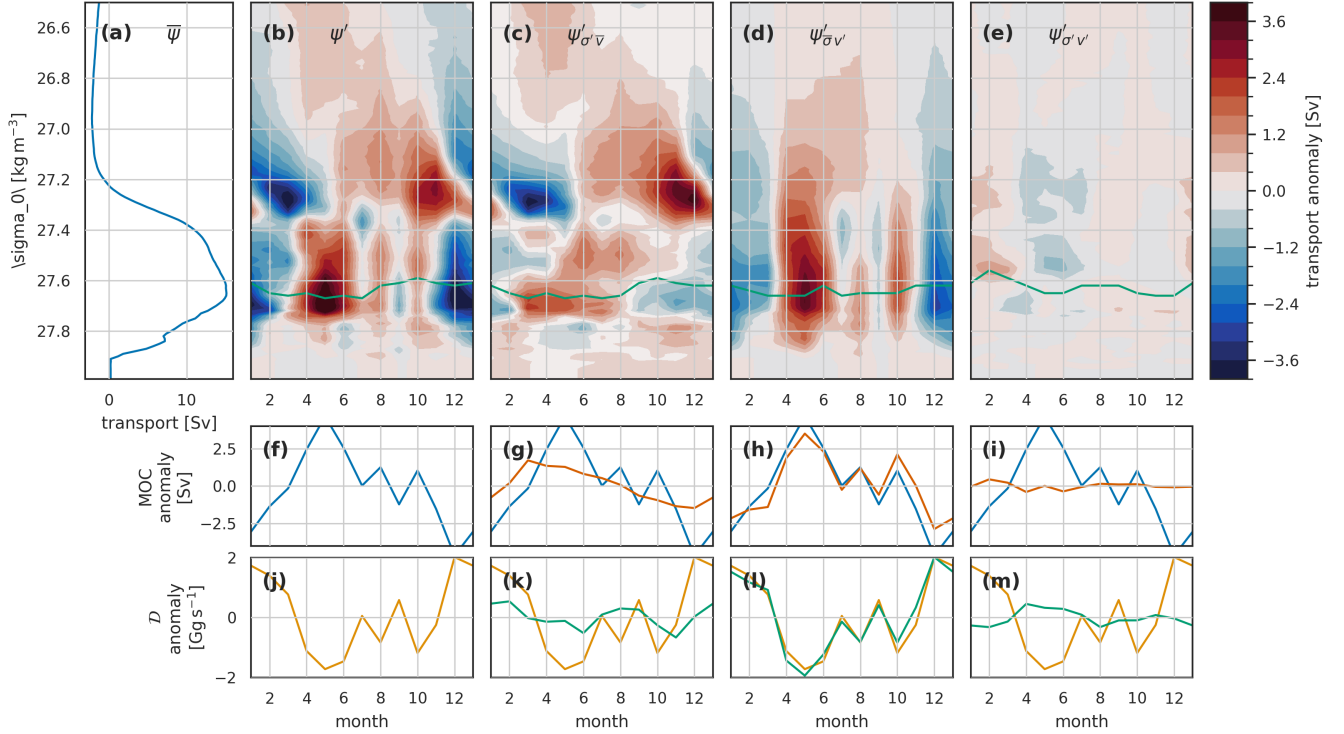
Figure 12. The seasonal cycle in the (a-e) overturning streamfunction Ψ, (f-i) MOC, and (j-m) density flux $\mathcal{D}$ for the full OSNAP transect in the **OSNAP observations**. Seasonal total anomalies (b,f,j) are decomposed into (c,g,k) density-driven, (d,h,l) velocity-driven and (e,i,m) covarying density-velocity components. See Fig. 4 for full details of the figure layout.

Comparing the observed seasonal cycle of the streamfunction (Fig. 12b-d) with the model (Fig. 4b-d) highlights many similarities but also notable differences. Perhaps ~~most noticeable~~ the most noticeable difference is the higher levels of high-frequency (month-to-month rather than seasonal) variability in the observations compared to the model. This high frequency signal is dominated by the velocity-driven component. This disparity is partly due to the shorter time period analysed in the observations (6 years as against 20 years in the model). To test this we repeated the model analysis using purely the

2014 to 2020 period to match the observations. While this produced a larger high-frequency signal than the 20 year model run it was still notably smaller than that in the observations~~and partly obscured the model signal~~, a subset of these results 6 year

440   model results are presented in the Supplementary Information, Figs. S1-S3.

Looking past this high-frequency signal to the seasonal signal we again see the dipole structure described in the model (Fig. 12b), though not as well-defined. At lower densities this is dominated by the density-driven anomalies (Fig. 12c) and in particular by the zonal mean near-surface density-driven anomalies (not shown). At higher densities, above and around the density of maximum overturning, this density-driven seasonal cycle (Fig. 12c) is somewhat weaker in the observations than in

445   the model.

The velocity-driven anomalies are stronger in the observations (Fig. 12d) than in the model (Fig. 4d), with a particularly strong maximum centred in May which is not really present in the modelled anomalies. This May maximum is mostly in the residual component, and is part of the higher-frequency signal described above.

The generally weaker density-driven and stronger velocity-driven seasonal cycles in the observed overturning streamfunction

450   are reflected in the meridional overturning (Fig. 12f-i) and density flux (Fig. 12j-m). Whereas in the model the density-driven component was the largest component of MOC_σ, in the observations the velocity-driven component is dominating both MOC and density flux.

Figure 13 breaks down the observed MOC and density flux into the various components (compare with Fig. 9). The observed MOC seasonal cycle, in contrast to the model, is dominated by the velocity-driven anomalies. These anomalies are a combina-

455   tion of the annual cycle of surface Ekman-driven flows, with a minimum in the winter when the stronger wind-driven Ekman currents oppose the overturning, and residual flows. ~~These~~ The Ekman-driven seasonal variability is larger in the observations than in the model, this is largely due to the different time-periods covered. The 6 year model results (Figs. S1-S3), covering the same period as the observations, show a larger amplitude Ekman component than the 20 year model run, more in line with the observations, suggesting that this may be a result of interannual variability in the seasonal cycle of the winds. The

460   residual flows, generally showing higher-frequency variability, are notably larger in the observations than in the model. The density-driven part of the observed MOC seasonal cycle, as for the model, shows contributions from both temperature and salinity variability (Fig. 13a), though the observed variability due to salinity is shifted out of phase (lagging by 4 to 5 months). The density-driven MOC variability (Fig. 13b) has a larger contribution from the residual component than in the model.

The observed density flux seasonal cycle, as with the model, is dominated by the velocity driven variability (Fig. 13f), though

465   with generally larger contribution from ~~the residual component~~ both the residual and Ekman components than in the model. The density-driven component of the observed density flux seasonal cycle is relatively small and variable with no clearly dominant components (Fig. 13d,e). As for the model, the observed density flux seasonal cycle shows some opposition between temperature and salinity-driven signals.
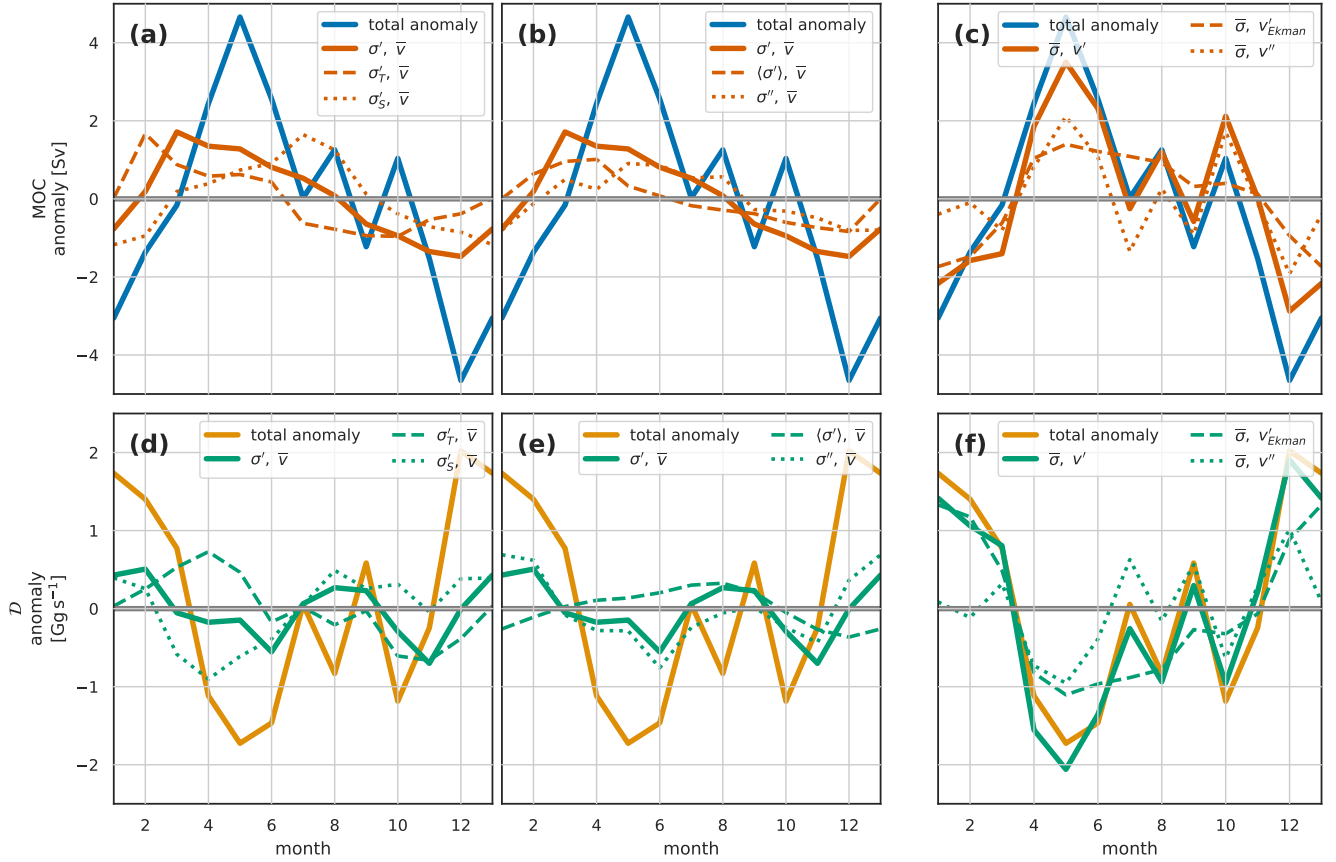
Figure 13. As for Fig 9 but for the **observed** seasonal cycle on the **full OSNAP section**.

3.2.2 OSNAP East and OSNAP West

470 For OSNAP$_E$, as for the full section, velocity-driven variability dominates both MOC and density flux seasonal cycles (Fig. 14). This velocity variability is a combination of seasonally varying Ekman transports and a high-frequency remainder. Though it forms the smaller part of the seasonal cycle, we look now at the density-driven variability in more detail.

A particular feature of the seasonal cycle of observed density-driven MOC in OSNAP$_E$, which isn't seen in the full OSNAP section, OSNAP$_W$ or the model, is the opposing contribution of temperature and salinity (Fig. 14a). We examine this in Fig. 15

475 where we plot the difference between the early spring and early autumn extremes of the seasonal cycle. ~~The~~

Evaluating Eq. 19 at $\sigma = \sigma_{\mathrm{MOC}}$, we see that the density-driven part of the seasonal cycle of MOC is entirely due to the seasonal cycle of the depth of σ_{MOC} ($z'(\sigma_{\mathrm{MOC}})$). And in particular how σ_{MOC} depth variability, which is a function of location (x), interacts with the local mean velocity field. This implies that, in Fig. 15a, the difference in density-driven MOC between these two seasonal extremes is purely due to the ~~volume transport~~ transport by the mean currents in the region between the

480 respective σ_{MOC} isopycnals. ~~Thus,~~ So we find the seasonal cycle of density-driven MOC in OSNAP$_E$ to be almost entirely due

to seasonal changes of near-surface density in the Irminger Basin ~~; a competition between northward transports in the eastern~~ ~~basin driving an~~ as elsewhere the seasonal vertical migration of σ_{MOC} is small. The resulting seasonal cycle in MOC, with a spring maximum and autumn minimum, is the result of a competition between the eastern Irminger Basin, where northward mean transports drive a spring minimum and autumn peak in MOC ~~(more northward flow in the lower limb reducing MOC in~~ ~~spring) and southward transports in~~ and the East Greenland Current ~~at~~ in the west of the ~~basin driving~~ Basin where southward mean transports drive a spring peak and autumn minimum. The resulting density-driven seasonal cycle is dominated by the cycle in the East Greenland Current. ~~This competition is 'won' by the southward flows, resulting in the observed spring peak.~~
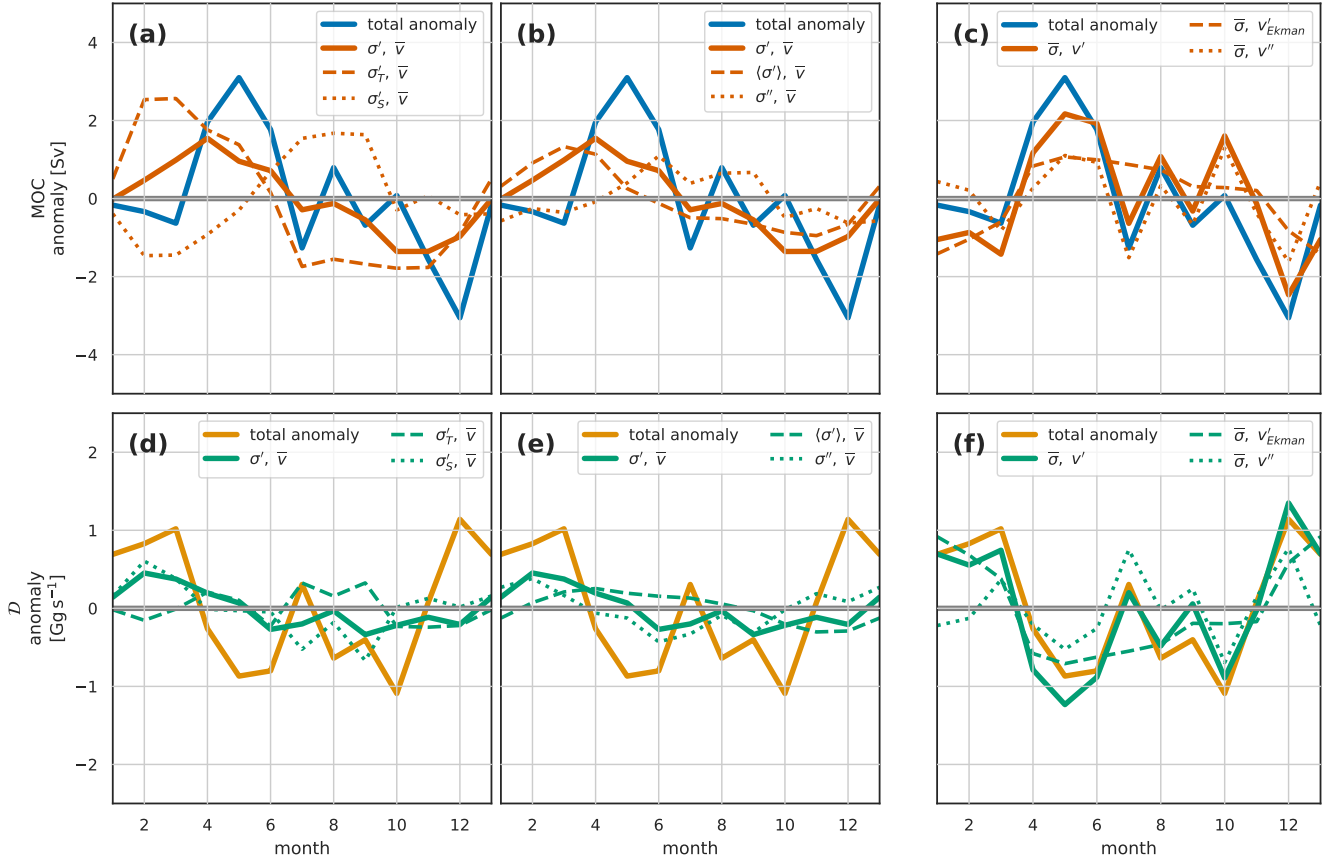
Figure 14. As for Fig 9 but for the **observed** seasonal cycle at **OSNAP$_{\text{E}}$**.

~~Panels b,c,d of~~ The dominant feature of seasonal density variation on OSNAP$_{\text{E}}$, Fig. 15~~illustrate how the density-driven~~ ~~seasonal cycle~~ b, is the basin-scale, near-surface seasonal cycle described earlier. This seasonal cycle in density produces a strong seasonal cycle in the depth of σ_{MOC}~~depth~~, and hence ~~of~~ large contributions to MOC ~~, is associated with the zonal-mean~~ ~~seasonal cycle of surface~~density seasonal variability, in regions where σ_{MOC} is close to the surface, that is in the Irminger ~~Basin. This~~ Sea. The basin-scale surface density signal is primarily driven by large-scale seasonal temperature variation ~~.~~
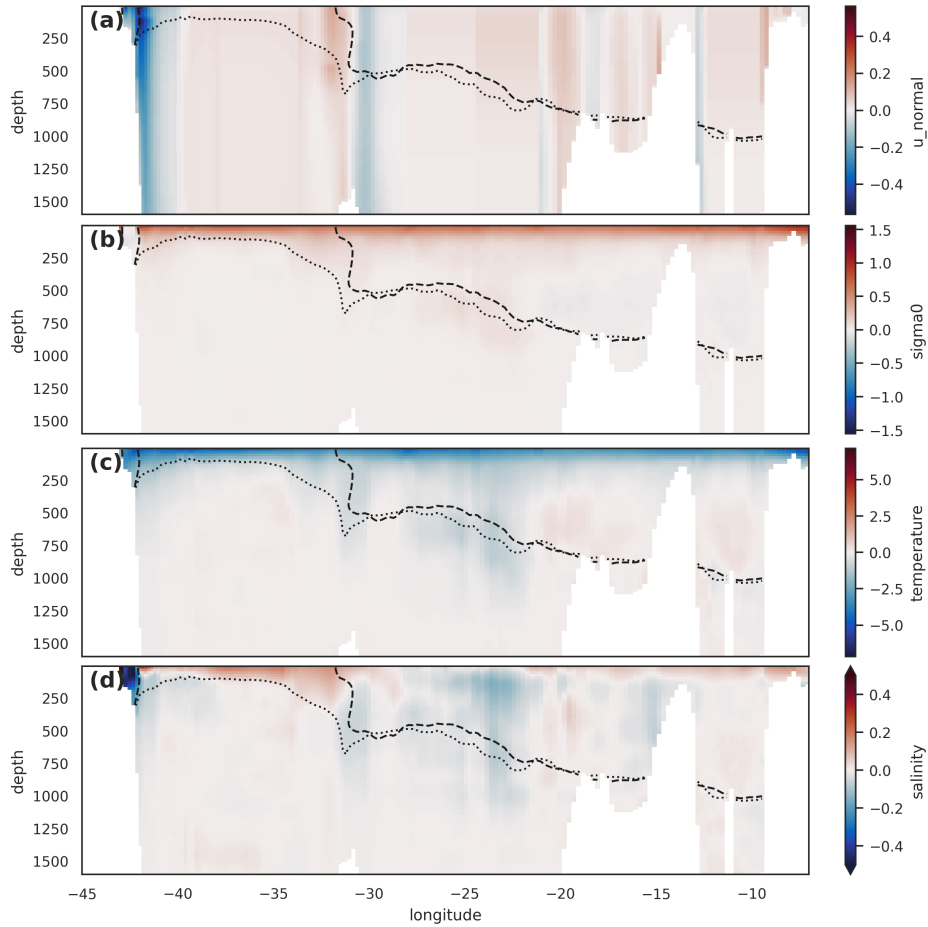
Figure 15. Observed OSNAP$_E$ density-driven seasonal cycle. (a) mean velocity normal to the section, with σ_{MOC} for April (dashed line) and October (dotted line) superimposed. These represent the observed extremes of the density-driven seasonal cycle of σ_{MOC}. (b,c,d) show the difference between water properties in April and October (shading,April minus October) for (a) density, (b) temperature and (c) salinity. The σ_{MOC} for April (dashed line) and October (dotted line) are superimposed in each case.

~~Over~~ Fig. 15c. In addition, over much of the Irminger Sea the seasonal signal of near-surface salinity~~supports~~, Fig. 15d, reinforces the temperature variation, ~~reducing density by~~ further reducing density in the autumn through seasonal ~~heating and~~

495 ~~freshening. The dominant opposing salinity-driven signal in~~ freshening. However, Fig. 14a ~~is more subtle, and is~~ showed the salinity-driven signal to oppose the temperature-driven signal. This opposing salinity-driven signal is due to a small region at the west of the section where the near-surface seasonal cycle of salinity is reversed ~~,~~ (small blue area in Fig. 15d), opposing the temperature-driven signal, with warm salty water present in the autumn. This dominates the salinity-driven seasonal cycle because of the strong southward currents. This feature is also present in the model but lies mostly outside the region ~~enslosed~~

500 enclosed by the seasonal variation of σ_{MOC}. This more detailed analysis of the observed density-driven MOC at OSNAP$_E$

highlights how variability in the MOC measure of meridional overturning can be dominated by very local changes in regions of strong flow.

Observations of MOC and density-flux at OSNAP$_W$ (Fig. ~~14~~16d-f) show generally smaller amplitude and less coherent seasonal signal than in model. Velocity-variation is dominant, as in all the observations, even with small Ekman contribution. The observed seasonal cycle of density flux again shows opposing temperature and salinity components as for the observed full OSNAP section and the model. ~~This opposition is a different mechanism to that for the OSNAP$_E$ MOC seasonal cycle described above as the density-driven density-flux variability samples the full density fields, not just the region bounded by extremes of σ_{MOC}.~~ As described previously (Sect. 3.1.1), this opposition of temperature and salinity in the density flux seasonal cycle is due to the temperature component being dominated by the seasonal heating and cooling in northward-flowing surface waters, while the strong seasonal summer freshening of the southward surface flow on the western boundary dominates the salinity component.
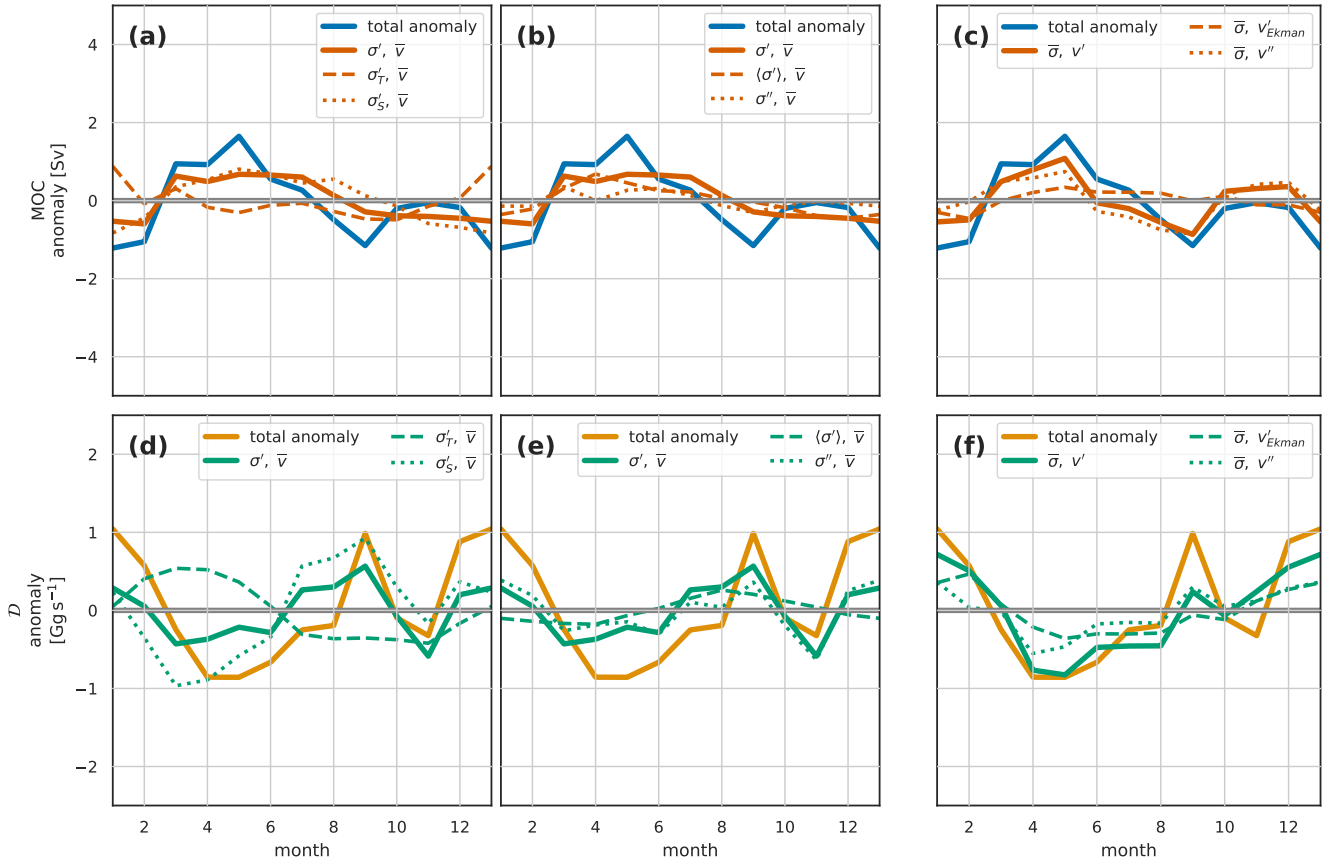
Figure 16. As for Fig 9 but for the **observed** seasonal cycle at **OSNAP$_W$**.

3.3 Seasonal cycles of heat and freshwater transport

We might expect, with small net throughflow, that the density fluxes (Figs. 9d-f and 13d-f) would be some form of weighted sum of the heat and freshwater fluxes (with sign reversed). This relationship is not immediately obvious from the heat and freshwater fluxes for either the model (Fig. 17) or observations (Fig. 18).
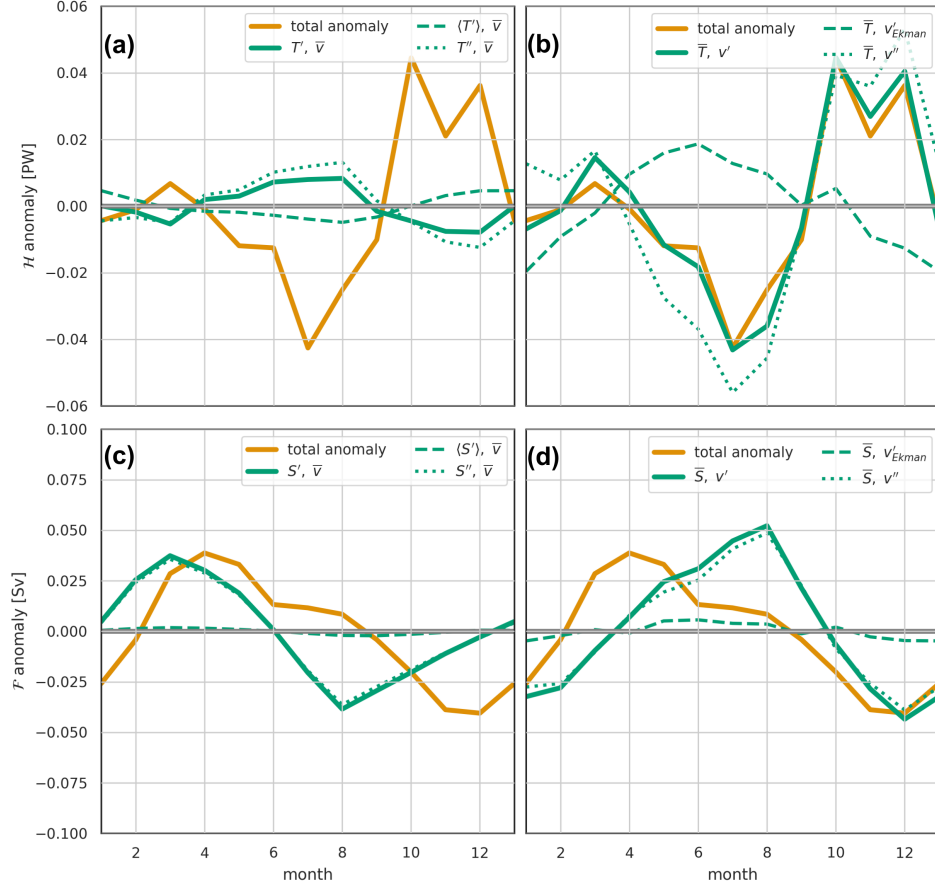
Figure 17. The **Modelled** OSNAP heat transport $\mathcal{H}$ (a,b) and freshwater transport $\mathcal{F}$ (c,d) seasonal cycle. (a) Seasonal heat transport anomalies driven by temperature variability, mean velocities: solid yellow line – total anomaly; solid green – total temperature-driven anomaly; dashed line – component due to zonal mean temperature variability; component due to residual temperature variability. (b) Seasonal heat transport anomalies driven by velocity variability, mean temperatures: solid yellow line – total anomaly; solid green – total velocity-driven anomaly; dashed line – component due to Ekman transport variability; component due to residual velocity variability. (c) Seasonal freshwater transport anomalies driven by salinity variability, mean velocities: solid yellow line – total anomaly; solid green – total salinity-driven anomaly; dashed line – component due to zonal mean salinity variability; component due to residual salinity variability. (b) Seasonal freshwater transport anomalies driven by velocity variability, mean salinities: solid yellow line – total anomaly; solid green – total velocity-driven anomaly; dashed line – component due to Ekman transport variability; component due to residual velocity variability.
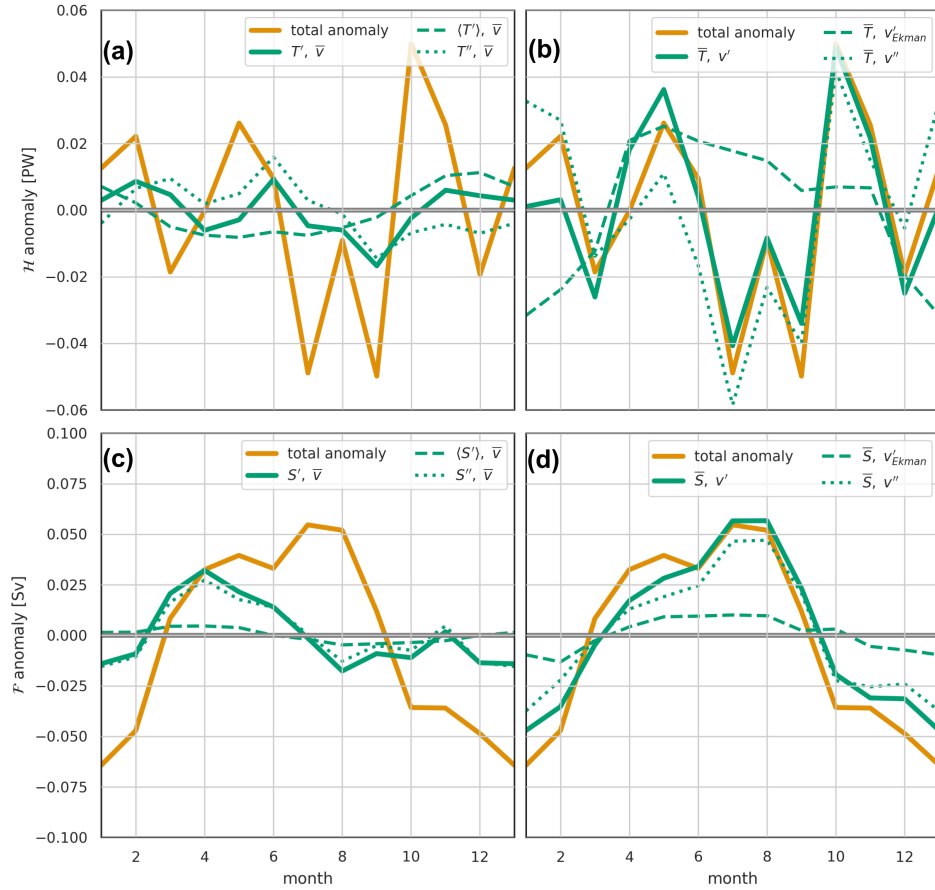
Figure 18. The **Observed** OSNAP heat transport $\mathcal{H}$ (a,b) and freshwater transport $\mathcal{F}$ (c,d) seasonal cycle. For a full description of the panels see Fig. 17.

Closer examination suggests that the fundamental shape of the seasonal cycle of density flux is being dominated by the freshwater flux. Both density and freshwater flux are predominantly southward through the year, the winter mimimum and spring-summer maximum in southward density flux correspond to winter maximum and spring-summer minimum in southward freshwater flux. The heat flux plays a more minor role, shifting the peak in the density flux and, particularly in the observational case, adding higher frequency variability. The principle complicating factor in relating heat and freshwater flux to density flux is the large variability of the thermal expansion coefficient with temperature – at low temperatures the same amount of added heat causes a much smaller change in density than at higher temperatures.

Examining the decomposition of heat transports into components driven by the seasonal cycle of temperature and velocity (Figs. 17a,b and 18a,b) we find that, as for density flux, the seasonal cycle of heat transports is dominated by the velocity variability acting on the mean temperature field. But, whereas for density flux the dominant velocity variability is surface Ekman, for heat transport the seasonal variability is dominated by the remainder term, predominantly variability in the barotropic flow.

In the observations, this barotropic velocity variability is also the source of the high-frequency variability in heat transport. As the driving velocity variability is the same for both heat transport and density flux, the difference in dominant velocity component – Ekman or barotropic – must be due to the interaction between the velocity variability the mean temperature or density fields.

For freshwater transport (Figs. 17c,d and 18c,d) the seasonal cycle is also, to a large extent, driven by the barotropic velocity variability. With peak southward freshwater transport in winter and minimum in late summer in both observations and model. In contrast to the heat transport, ~~the property variability~~ for freshwater transport the property-variability term (here, salinity) ~~is~~ also plays a role (Figs. 17c and 18c) ~~acting to shift the~~ having similar magnitude to the velocity-driven term. This shifts the phase of the seasonal cycle of freshwater transport earlier in the year, with a spring minimum in southward freshwater transport and late summer/autumn maximum. This phase corresponds to the seasonal cycle of freshwater exiting southwards across the OSNAP line in the near-surface western boundary current. Notice that the salinity-driven variability lies entirely in our remainder term - rather than in the zonal-averaged salinity variability. This ~~is because the largest~~ remainder term contains the horizontal structure of salinity variability. Fig. 15d, for OSNAP$_E$, showed more horizontal structure in salinity variability than for either temperature or density, the same holds true for the full OSNAP section. The strongest seasonal salinity variability is ~~confined to the southward flow at the~~ found near-surface in the western boundaries, rather than ~~the broader zonal horizontal scale of surface temperature seasonal variability~~ over the broad zonal horizontal scales. Coupled with the strong currents, this western boundary variability dominates the salinity-driven part of the seasonal freshwater transport signal.

4   Discussion

We have examined the seasonal cycle of subpolar North Atlantic overturning in the overturning streamfunction and four associated metrics: the commonly used meridional overturning, MOC (the maximum of the streamfunction Ψ); heat transport and freshwater transport; and the less commonly considered density flux. We have looked at each of these in an eddy-resolving model and in observational data from the OSNAP array. We have further divided these metrics into separate components driven by velocity and density variability. We have attempted to place these metrics in a coherent framework, particularly highlighting the relationship of the MOC and the density flux to the overturning streamfunction. The main results are summarised in Sect. 5, here we consider the following questions in a little more depth: Is the density-flux a useful (additional) metric for monitoring overturning? What may cause the differences between modelled and observed seasonal cycles? How do our results complement and advance previous studies of the seasonal cycles of subpolar overturning? What are the implications, if any, for the monitoring and study of lower frequency variability of the overturning circulation?

Firstly, the density flux. For the seasonal cycle each of the metrics considered is dominated by a different physical process or region. For example for the full OSNAP section seasonal cycle: MOC is mostly responding to a combination of the near-surface density in the western boundary current and Ekman transport variability; density flux is dominated by Ekman transport variability; heat flux by variability of non-Ekman, mostly barotropic, residual velocities; and freshwater flux responds to a combination of the barotropic velocities and the seasonal cycle of surface salinity in the western boundary. The density flux

560 may not therefore appear very useful – mostly responding to the Ekman transport variability. However, this is largely due to the cancellation of density-driven seasonality in the density flux between $OSNAP_E$ and $OSNAP_W$, temperature variability dominating in $OSNAP_E$ while salinity variability dominates in $OSNAP_W$. As an integrated measure, rather than an extreme, density-flux is arithmetically 'better' behaved than MOC: ~~density fluxes sums, averages,~~ averages, sums, trends and variability of density flux are simple to calculate; ~~unlike~~ MOC ~~which needs to~~ however must always be considered in the context of the

565 changing σ_{MOC} value ~~and, where possible analysis undertaken on the full streamfunction before calculating~~ – for example the annual mean MOC is not the same as the mean of the monthly MOCs as each monthly maximum will occur at a different σ_{MOC}. The MOC metric, at least for the seasonal cycle, is ~~also~~ found to be extremely sensitive to ~~variability in a~~ density variation in very limited geographic ~~region~~ regions – for example MOC variability in $OSNAP_E$ is found to be ~~entirely due to~~ dominated by surface temperature variability in the Irminger basin and the East Greenland Current ~~whereas density flux~~

570 ~~is sampling~~ where the σ_{MOC} isopycnal is close to the surface. Meanwhile, the density flux appears to be a more balanced measure, responding to multiple processes across the whole basin~~including the North Atlantic Current~~. We might even conclude that the current focus of many overturning studies on the Irminger Basin and East Greenland Current is as much a function of the characteristics of the MOC metric as of the importance of these regions to overturning. Density flux turns out not to be a simple combination of heat and freshwater flux, this is highlighted here as both heat and freshwater flux seasonality

575 are strongly influenced by the barotropic velocity variability, which plays only a minor part in the density flux seasonality. We suggest that density flux complements the more commonly used overturning metrics and as such would recommend that density flux becomes a routinely used additional metric, if not the primary metric, when studying the overturning circulation.

While modelled and observed seasonal cycles are largely consistent there are some differences. The observations show a larger Ekman-driven seasonal cycle, this is primarily due to the different averaging periods for the model and observations.

580 When the model analysis is repeated on the observational time period the Ekman component is correspondingly stronger (Figs. S1-S3). The modelled seasonal cycles of both MOC and density flux show a larger contribution from the density-driven variability than the observations. Some of this is due to a weaker freshwater cycle in the model (the freshwater-driven overturning often opposes the heat-driven overturning), and some to a stronger seasonal cycle of near-surface temperature in the model, particularly in $OSNAP_E$. This may be a function of the surface forcing dataset used in the Viking20x model, or

585 alternatively an underestimate of the seasonal cycle of surface tenperature in the observations. We have shown how the MOC metric is extremely sensitive to temperature and salinity variability in quite confined regions of strong flow near the surface. Finally, and perhaps the largest difference between model and observational seasonal cycles, is the presence of high-frequency variability, particularly evident in the non-Ekman-driven velocity component in the observations. This is centred in $OSNAP_E$ and in the barotropic velocities. ~~Only a~~ A small part of this high-frequency variability is due to the shorter period spanned

590 by the observations (see Figs. S1-S3)~~. This could be associated with missing model physics~~, the rest may be due to missing physics in the model, or the difficulty making high-quality observations of ~~the~~ barotropic currents with limited resources. ~~The OSNAP gridding methodology, away from the boundary regions, assumes spatially-uniform barotropic velocities calculated as a volume-balance compensation velocity, these can involve rapidly-varying transports of tens of Sverdrups though we haven't been able to link this directly to the high-frequency variability observed here.~~

Observational and modelling studies of subpolar North Atlantic meridional overturning consistently return estimates of the seasonal cycle of overturning, as measured by the maximum of the overturning streamfunction (MOC_σ), with amplitude of about 4 Sv with a late spring maximum and autumn or winter minimum ~~(Lozier et al., 2019; Fu et al., 2023; Wang et al., 2021; Tooth et al.,~~ (Lozier et al., 2019; Wang et al., 2021; Fu et al., 2023; Tooth et al., 2023; Mercier et al., 2024). Our results, both model and observational, confirm these general conclusions.

Published analyses, both model-based and observational, tend to focus on MOC seasonality, predominantly in the eastern subpolar gyre (OSNAP$_\text{E}$ and OVIDE). These show the subpolar AMOC seasonal cycle to be dominated by seasonality in the Irminger Basin, particularly the East Greenland Current, modified by Ekman transport driven by seasonality in the zonal winds (Wang et al., 2021; Fu et al., 2023; Tooth et al., 2023; Mercier et al., 2024). Observational (Le Bras et al., 2018; Mercier et al., 2024) and model (Tooth et al., 2023) analyses find the MOC variability due to the East Greenland Current to be a combination of density-field and transport variability - though it is difficult to disentangle the two due to the dominance of geostrophic currents. The results we obtain generally confirm the importance of Ekman and western boundary processes in the seasonality of MOC. However, we find little contribution from western boundary transports in either models or observations; the western boundary contribution to MOC being almost entirely explained by the zonal mean density variability. This is particularly notable because this zonal mean density variability has no associated zonal pressure gradients, so is uncoupled from the velocity fields.

The Irminger Basin and East Greenland Current density and transport seasonality have been ascribed to a lagged signal of watermass transformation and North Atlantic deep water (NADW) formation in the Irminger Basin (Fu et al., 2023), with the relatively short lag time attributed to the travel time from the transformation regions to OSNAP$_\text{E}$ (Le Bras et al., 2020; Fu et al., 2023). However Tooth et al. (2023) points out that the 4 Sv seasonal signal in overturning is much smaller than the 20 Sv seasonality in the watermass transformation in the Irminger Basin north of OSNAP$_\text{E}$, the difference between the two being seasonal heat storage and release from the surface waters. While we don't disagree with this lagged transformation diagnosis, we note that the seasonality of MOC is tied to the seasonality of the surface density structure, mostly summer/autumn warming and winter/spring cooling. This seasonality naturally lags the water transformation cycle which is tied to the surface fluxes, mostly due to the large heat capacity of seawater and vertical mixing. Given the basin-scale nature of the surface density cycle, and the similar large scale of seasonal surface heat fluxes (e.g. Berry and Kent, 2009) the simpler explanation of seasonal rise and fall of the σ_MOC isopycnal due to the local seasonal cycle of surface fluxes is perhaps more appropriate than that of advectively lagged water transformation. We note that advection certainly has a role in surface flux effects on density, but the estimated seasonal advective distances involved in even the fastest currents in the region (8 months around the northern segment of the Irminger Basin Tooth et al., 2023) are still relatively small compared to the length scales of seasonal surface fluxes.

We must emphasise that the location of the dominant OSNAP$_\text{E}$ overturning seasonality in the East Greenland Current is not new, it confirms the results of Wang et al. (2021); Fu et al. (2023); Tooth et al. (2023); Mercier et al. (2024). However we also emphasise that this local dominance is partly a feature of the MOC metric, since density, heat and freshwater flux seasonal cycles are less dominated by this single small region. The Irminger Basin and East Greenland Current dominance of the MOC

seasonal cycle is due to a combination of two factors – the dominance of the cycle by near-surface seasonal density variability, and this region being the only part of OSNAP$_\text{E}$ where the σ_MOC isopycnal is within the depth range of this surface ~~variability.~~ density variability (Fig. 15). MOC needs to be carefully interpreted in the context of σ_MOC position and variability.

While these comparisons, and the exploration of mechanisms driving seasonality of the MOC overturning metric are enlightening, the more interesting result is how poorly the MOC metric seasonal cycle predicts the seasonal cycle in any of the integrated metrics – density, heat and freshwater fluxes – mostly due to its high sensitivity to a small set of processes in a limited geographical region. It is these integrated metrics, and how they evolve, which are arguably more relevant to understanding the potential changes to overturning seasonality which are most important for mitigating the impacts of AMOC changes on Atlantic sector weather and climate.

We now consider how our conclusions from analysis of the seasonal cycles may be extended to longer-term monitoring of the Atlantic meridional overturning circulation. The model-observation seasonal cycle differences require consideration from both large-scale overturning observational and modelling perspectives to improve confidence in observations and predictions of overturning. The largest differences found were in the representation of barotropic currents and near-surface seasonal temperature and salinity structures – particularly in the boundary currents – at depths which may be shallower than the upper sensors on longterm monitoring arrays. Both of these differences suggest possible focusses for improvement of long-term AMOC monitoring and climate modelling. Further, MOC is commonly used for climate model verification, however a focus on reproducing the MOC metric may be a poor guide to the quality of the modelled overturning circulation and property fluxes.

We find the most commonly considered MOC metric – the maximum of the overturning streamfunction – to be overly focussed on seawater property changes in a couple of small geographic regions: flows in the upper 500 m in the East Greenland Current and 1000 m in the Labrador Current. This is certainly the case on seasonal timescales, it may be a more reliable metric on longer timescales but this needs to be demonstrated. We also note that while OSNAP$_\text{E}$ makes the largest contribution to all the metrics (except freshwater flux), focus on MOC perhaps exaggerates the comparative importance of OSNAP$_\text{E}$ versus OSNAP$_\text{W}$ to the overturning circulation and its wider implications; and within OSNAP$_\text{E}$ MOC probably underemphasises the importance of the northward flows of warm and salty waters in the eastern subpolar gyre (Iceland Basin and Rockall Trough) to the overturning. We need to be mindful of all these characteristics of the MOC metric when designing observational campaigns.

~~Heat and freshwater fluxes must also not be neglected as measures of overturning, our analysis finds these to be strongly influenced by the barotropic current variability . These barotropic currents are the currents which OSNAP (and RAPID) are most likely to get wrong, because the barotropic compensation transport is applied quite crudely. We suggest that this could specifically affect the accuracy of observed heat and freshwater flux estimates, while still appearing to get the right answer for MOC~~

While extrapolating from the present work on seasonal variability to longer timescales is difficult, the characteristics of *MOC* metric seasonal variability — the domination of the metric by movement a single density interface — are not obviously specific to short timescales. In recent work Chafik and Lozier (2025) raise similar concerns about the use of the MOC metric, concluding that it essentially captures variability in upper ocean heat content, which can result from a number of mechanisms, some unrelated to overturning. Models of overturning slowdown (see for example Baker et al., 2025) show a combination of

reduced volume transformation across the density of maximum overturning (sampled by the MOC metric), changing density of maximum overturning (often ignored), and reduced density difference between northward and southward flows (not sampled by MOC). There is a ~~real danger that excessive, or exclusive~~ risk that exclusive, or excessive, focus on MOC ~~could miss overturning 'slowdown' associated with unsampled variability~~ in both modelling and observations could underestimate the long-term societally relevant AMOC decline, for example ~~,~~ by missing decline associated with a changing density difference between upper and lower limbs ~~rather than reduced net transport~~ (Koman et al., 2024). The ~~addition of~~ use of the density flux metric ~~would~~ alongside MOC could help capture such changes while requiring no additional observations.

Heat and freshwater fluxes must also not be neglected as measures of overturning, though our analysis finds these to be strongly influenced by the barotropic current variability, including large high-frequency variability particularly evident in the observations. These barotropic currents are perhaps the currents with the largest uncertainty in basin-wide overturning estimates. The barotropic velocity component is generally partly composed of a uniform 'compensation' velocity applied to control the total transport through the section. While this compensation involves small velocities it can integrate to several tens of Sverdrups of transport. The compensation velocity problem has been widely considered (Bryden and Hall, 1980; Lee and Marotzke, 199? though we could find no published literature specific to the OSNAP section. McCarthy et al. (2015) considered the application of the compensation velocity at RAPID, 26° N in the North Atlantic, they find the application of different compensation velocity structures doesn't have much impact on the vertical structure of the MOC streamfunction. The zonal structure of the barotropic component may be more important at OSNAP, interacting with larger interior variability in density structure (see, for example the different σ_{MOC} depth between the Irminger and Iceland basins, Fig. 15).

5 Conclusions

We place meridional overturning and density, heat and freshwater fluxes in a coherent framework. This framework highlights the integral relationship between meridional overturning circulation and property transports, both being functions purely of the overturning streamfunction Ψ. Using this framework we examine the seasonality observed in overturning and density, temperature and freshwater fluxes at the OSNAP line in the subpolar North Atlantic. We find MOC seasonal cycles to be dominated by Ekman transports and large-scale seasonal cycle of surface density; heat flux seasonal cycles to be dominated by barotropic velocity variability; freshwater fluxes by a combination of barotropic velocities and the salinity in the western boundary current; and density fluxes to reflect a broad range of processes. We further show that the standard measure of overturning, the MOC metric, is a poor predictor, on seasonal time-scales, of either density fluxes or the more societally relevant ocean heat and freshwater transports. This is due to each of these metrics responding to different physical processes. The MOC metric in particular has very high sensitivity to near-surface physical processes in a limited geographical area. These processes are not necessarily reflective of ~~the fundamental processes driving overturning. We find there to be a real danger~~ either the fundamental, or most societally relevant, characteristics of large-scale overturning. While extrapolating from the present work on seasonal variability to longer timescales is difficult, there are enough parallels for us to consider that there is a risk that exclusive focus on MOC could, for example, miss overturning 'slowdown' associated ~~unsampled variability,~~

for example, with a changing density difference ~~with changing density difference~~ with changing density differences between upper and lower limbs~~rather than reduced net transport (Koman et al., 2024)~~. The addition of use of the density flux metric would help capture such changes. Our results complement recent work of Chafik and Lozier (2025) who raise similar concerns about the ~~use~~ characteristics of the MOC metric. ~~We~~ Hence, we suggest caution in the exclusive use of the standard MOC metric in studies of overturning and recommend the routine use of the density flux as a valuable additional metric.

Code/data availability

Code and data availability. ERA5 monthly averaged data on single levels from 1940 to present were obtained from Copernicus Climate Change Service (C3S) Climate Data Store (CDS) https://doi.org/10.24381/cds.f17050d7 (Hersbach et al., 2023) (Last accessed on 5-Oct-2024). Neither the European Commission nor ECMWF is responsible for any use that may be made of the Copernicus information or data it contains. The OSNAP data were downloaded from https://doi.org/10.35090/gatech/70342 (last accessed 3-Dec-2024). OSNAP data were collected and made freely available by the OSNAP (Overturning in the Subpolar North Atlantic Program) project and all the national programs that contribute to it (Fu et al., 2023). VIKING20X-JRA-short data is available at https://doi.org/10.26050/WDCC/VIKING20XJRAshort (Getzlaff and Schwarzkopf, 2024). The python code and the small subset of Viking20x data used to perform the analysis described was written in Jupyter notebooks in Python and is available from https://doi.org/10.5281/zenodo.15350863 (Fox, 2025).

Author contribution

Author contributions. ADF defined the overall research problem, the methodology and performed the analyses. All co-authors discussed and refined the analyses and contributed to the text.

6 Competing interests

Competing interests. There are no competing interests

Acknowledgements

Acknowledgements. This work was supported by the UK Natural Environment Research Council (NERC) grants UK-OSNAP (NE/K010875/2), UK-OSNAP-Decade (NE/T00858X/1), and SNAP-DRAGON (NE/T013494/1), and by the NERC National Capability programme CLASS (NE/R015953/1). The ocean model simulation VIKING20X-JRA-short was performed at the North German Supercomputing Alliance (HLRN).

References

Baker, J. A., Bell, M. J., Jackson, L. C., Renshaw, R., Vallis, G. K., Watson, A. J., and Wood, R. A.: Overturning pathways control AMOC weakening in CMIP6 models, Geophys. Res. Lett., 50, e2023GL103 381, https://doi.org/10.1029/2023gl103381, publisher: John Wiley and Sons Inc, 2023.

Baker, J. A., Bell, M. J., Jackson, L. C., Vallis, G. K., Watson, A. J., and Wood, R. A.: Continued Atlantic overturning circulation even under climate extremes, Nature, 638, 987–994, https://doi.org/10.1038/s41586-024-08544-0, publisher: Nature Research, 2025.

Berry, D. I. and Kent, E. C.: A New Air–Sea Interaction Gridded Dataset from ICOADS With Uncertainty Estimates, Bulletin of the American Meteorological Society, 90, 645–656, https://doi.org/10.1175/2008BAMS2639.1, publisher: American Meteorological Society, 2009.

Biastoch, A., Schwarzkopf, F. U., Getzlaff, K., Rühs, S., Martin, T., Scheinert, M., Schulzki, T., Handmann, P., Hummels, R., and Böning, C. W.: Regional imprints of changes in the Atlantic Meridional Overturning Circulation in the eddy-rich ocean model VIKING20X, Ocean Science, 17, 1177–1211, https://doi.org/10.5194/os-17-1177-2021, publisher: Copernicus GmbH, 2021.

Bryden, H. L. and Hall, M. M.: Heat Transport by Currents Across 25°N Latitude in the Atlantic Ocean, Science, 207, 884–886, https://doi.org/10.1126/science.207.4433.884, publisher: American Association for the Advancement of Science, 1980.

Böning, C. W., Behrens, E., Biastoch, A., Getzlaff, K., and Bamber, J. L.: Emerging impact of Greenland meltwater on deepwater formation in the North Atlantic Ocean, Nature Geoscience, 9, 523–527, https://doi.org/10.1038/ngeo2740, publisher: Nature Publishing Group, 2016.

Chafik, L. and Lozier, M. S.: When Simplification Leads to Ambiguity: A Look at Two Ocean Metrics for the Subpolar North Atlantic, Geophysical Research Letters, 52, e2024GL112 496, https://doi.org/10.1029/2024GL112496, publisher: John Wiley & Sons, Ltd, 2025.

Chidichimo, M. P., Kanzow, T., Cunningham, S. A., Johns, W. E., and Marotzke, J.: The contribution of eastern-boundary density variations to the Atlantic meridional overturning circulation at 26.5° N, Ocean Science, 6, 475–490, https://doi.org/10.5194/OS-6-475-2010, publisher: Copernicus GmbH, 2010.

Cunningham, S. A., Kanzow, T., Rayner, D., Baringer, M. O., Johns, W. E., Marotzke, J., Longworth, H. R., Grant, E. M., Hirschi, J. J., Beal, L. M., Meinen, C. S., and Bryden, H. L.: Temporal variability of the Atlantic meridional overturning circulation at 26.5°N, Science, 317, 935–938, https://doi.org/10.1126/science.1141304, publisher: American Association for the Advancement of Science, 2007.

Forget, G., Campin, J. M., Heimbach, P., Hill, C. N., Ponte, R. M., and Wunsch, C.: ECCO version 4: An integrated framework for nonlinear inverse modeling and global ocean state estimation, Geoscientific Model Development, 8, https://doi.org/10.5194/gmd-8-3071-2015, 2015.

Fox, A. D.: Python code and data for producing the results described in: Seasonality of meridional overturning in the subpolar North Atlantic: implications for relying on the streamfunction maximum as a metric of AMOC slowdown., https://doi.org/10.5281/zenodo.15350863, 2025.

Fraser, N. J. and Cunningham, S. A.: 120 Years of AMOC Variability Reconstructed From Observations Using the Bernoulli Inverse, Geophysical Research Letters, 48, e2021GL093 893, https://doi.org/10.1029/2021GL093893, publisher: John Wiley & Sons, Ltd ISBN: 10.1029/2021, 2021.

Fraser, N. J., Fox, A. D., Cunningham, S. A., Rath, W., Schwarzkopf, F. U., and Biastoch, A.: Vertical Velocity Dynamics in the North Atlantic and Implications for AMOC, Journal of Physical Oceanography, 54, 2011–2024, https://doi.org/10.1175/JPO-D-23-0229.1, publisher: American Meteorological Society, 2024.

Fraser, N. J., Fox, A. D., and Cunningham, S. A.: Impact of Ekman Pumping on the Meridional Coherence of the AMOC, Geophysical Research Letters, 52, e2024GL108 846, https://doi.org/10.1029/2024GL108846, publisher: John Wiley & Sons, Ltd, 2025.

760 Fu, Y., Lozier, M. S., Biló, T. C., Bower, A. S., Cunningham, S. A., Cyr, F., de Jong, M. F., deYoung, B., Drysdale, L., Fraser, N., Fried, N., Furey, H. H., Han, G., Handmann, P., Holliday, N. P., Holte, J., Inall, M. E., Johns, W. E., Jones, S., Karstensen, J., Li, F., Pacini, A., Pickart, R. S., Rayner, D., Straneo, F., and Yashayaev, I.: Seasonality of the Meridional Overturning Circulation in the subpolar North Atlantic, Communications Earth & Environment 2023 4:1, 4, 1–13, https://doi.org/10.1038/s43247-023-00848-9, publisher: Nature Publishing Group, 2023.

765 Gary, S. F., Cunningham, S. A., Johnson, C., Houpert, L., Holliday, N. P., Behrens, E., Biastoch, A., and Böning, C. W.: Seasonal cycles of oceanic transports in the eastern subpolar North Atlantic, Journal of Geophysical Research: Oceans, 123, 1471–1484, https://doi.org/10.1002/2017JC013350, publisher: John Wiley & Sons, Ltd, 2018.

Getzlaff, K. and Schwarzkopf, F. U.: VIKING20X-JRA-short: daily to multi-decadal ocean dynamics under JRA55-do atmospheric forcing., https://doi.org/10.26050/WDCC/VIKING20XJRAshort, world Data Center for Climate (WDCC) at DKRZ, 2024.

770 Han, L.: Exploring the AMOC Connectivity Between the RAPID and OSNAP Lines With a Model-Based Data Set, Geophysical Research Letters, 50, e2023GL105 225, https://doi.org/10.1029/2023GL105225, publisher: John Wiley & Sons, Ltd, 2023a.

Han, L.: Mechanism on the Short-Term Variability of the Atlantic Meridional Overturning Circulation in the Subtropical and Tropical Regions, Journal of Physical Oceanography, 53, 2231–2244, https://doi.org/10.1175/JPO-D-23-0027.1, publisher: American Meteorological Society, 2023b.

775 Hersbach, H., Bell, B., Berrisford, P., Hirahara, S., Horányi, A., Muñoz-Sabater, J., Nicolas, J., Peubey, C., Radu, R., Schepers, D., Simmons, A., Soci, C., Abdalla, S., Abellan, X., Balsamo, G., Bechtold, P., Biavati, G., Bidlot, J., Bonavita, M., De Chiara, G., Dahlgren, P., Dee, D., Diamantakis, M., Dragani, R., Flemming, J., Forbes, R., Fuentes, M., Geer, A., Haimberger, L., Healy, S., Hogan, R. J., Hólm, E., Janisková, M., Keeley, S., Laloyaux, P., Lopez, P., Lupu, C., Radnoti, G., de Rosnay, P., Rozum, I., Vamborg, F., Villaume, S., and Thépaut, J. N.: The ERA5 global reanalysis, Quarterly Journal of the Royal Meteorological Society, 146, 1999–2049, 780 https://doi.org/10.1002/QJ.3803, publisher: John Wiley & Sons, Ltd, 2020.

Hersbach, H., Bell, B., Berrisford, P., Biavati, G., Horányi, A., Muñoz-Sabater, J., Nicolas, J., Peubey, C., Radu, R., Rozum, I., Schepers, D., Simmons, A., Soci, C., Dee, D., and Thépaut, J.-N.: ERA5 monthly averaged data on single levels from 1940 to present, https://doi.org/10.24381/cds.f17050d7, publication Title: Copernicus Climate Change Service (C3S) Climate Data Store (CDS), 2023.

Hirschi, J. J., Barnier, B., Böning, C., Biastoch, A., Blaker, A. T., Coward, A., Danilov, S., Drijfhout, S., Getzlaff, K., Griffies, S. M., 785 Hasumi, H., Hewitt, H., Iovino, D., Kawasaki, T., Kiss, A. E., Koldunov, N., Marzocchi, A., Mecking, J. V., Moat, B., Molines, J. M., Myers, P. G., Penduff, T., Roberts, M., Treguier, A. M., Sein, D. V., Sidorenko, D., Small, J., Spence, P., Thompson, L. A., Weijer, W., and Xu, X.: The Atlantic Meridional Overturning Circulation in High-Resolution Models, Journal of Geophysical Research: Oceans, 125, https://doi.org/10.1029/2019JC015522, publisher: Blackwell Publishing Ltd, 2020.

Johnson, H. L., Cessi, P., Marshall, D. P., Schloesser, F., and Spall, M. A.: Recent Contributions of Theory to Our Understanding of the Atlantic Meridional Overturning Circulation, Journal of Geophysical Research: Oceans, 124, 5376–5399, 790 https://doi.org/10.1029/2019JC015330, publisher: John Wiley & Sons, Ltd, 2019.

Kanzow, T., Cunningham, S. A., Rayner, D., Hirschi, J. J., Johns, W. E., Baringer, M. O., Bryden, H. L., Beal, L. M., Meinen, C. S., and Marotzke, J.: Observed flow compensation associated with the MOC at 26.5°N in the Atlantic, Science, 317, 938–941, https://doi.org/10.1126/science.1141293, publisher: American Association for the Advancement of Science, 2007.

795 Killworth, P. D.: A Simple Linear Model of the Depth Dependence of the Wind-Driven Variability of the Meridional Overturning Circulation, Journal of Physical Oceanography, https://doi.org/10.1175/2007JPO3811.1, 2008.

Koman, G., Bower, A. S., Holliday, N. P., Furey, H. H., Fu, Y., and Biló, T. C.: Observed decrease in Deep Western Boundary Current transport in subpolar North Atlantic, Nature Geoscience 2024 17:11, 17, 1148–1153, https://doi.org/10.1038/s41561-024-01555-6, publisher: Nature Publishing Group, 2024.

800 Le Bras, I. A., Straneo, F., Holte, J., de Jong, M. F., and Holliday, N. P.: Rapid Export of Waters Formed by Convection Near the Irminger Sea's Western Boundary, Geophysical Research Letters, 47, e2019GL085 989, https://doi.org/10.1029/2019GL085989, publisher: John Wiley & Sons, Ltd, 2020.

Le Bras, I. A. A., Straneo, F., Holte, J., and Holliday, N. P.: Seasonality of Freshwater in the East Greenland Current System From 2014 to 2016, Journal of Geophysical Research: Oceans, 123, 8828–8848, https://doi.org/10.1029/2018JC014511, publisher: John Wiley & Sons, 805 Ltd, 2018.

Lee, T. and Marotzke, J.: Seasonal Cycles of Meridional Overturning and Heat Transport of the Indian Ocean, Journal of Physical Oceanography, https://journals.ametsoc.org/view/journals/phoc/28/5/1520-0485_1998_028_0923_scomoa_2.0.co_2.xml, 1998.

Lozier, M. S., Li, F., Bacon, S., Bahr, F., Bower, A. S., Cunningham, S. A., de Jong, M. F., de Steur, L., DeYoung, B., Fischer, J., Gary, S. F., Greenan, B. J. W., Holliday, N. P., Houk, A., Houpert, L., Inall, M. E., Johns, W. E., Johnson, H. L., Johnson, C., Karstensen, J., Koman, 810 G., Le Bras, I. A., Lin, X., Mackay, N., Marshall, D. P., Mercier, H., Oltmanns, M., Pickart, R. S., Ramsey, A. L., Rayner, D., Straneo, F., Thierry, V., Torres, D. J., Williams, R. G., Wilson, C., Yang, J., Yashayaev, I., and Zhao, J.: A sea change in our view of overturning in the subpolar North Atlantic, Science, 363, 516+, https://doi.org/10.1126/science.aau6592, publisher: AMER ASSOC ADVANCEMENT SCIENCE Place: 1200 NEW YORK AVE, NW, WASHINGTON, DC 20005 USA, 2019.

Madan, G., Gjermundsen, A., Iversen, S. C., and LaCasce, J. H.: The weakening AMOC under extreme climate change, Clim. Dyn., 62, 815 1291–1309, https://doi.org/10.1007/s00382-023-06957-7, publisher: Springer Science and Business Media Deutschland GmbH, 2023.

McCarthy, G. D., Smeed, D. A., Johns, W. E., Frajka-Williams, E., Moat, B. I., Rayner, D., Baringer, M. O., Meinen, C. S., Collins, J., and Bryden, H. L.: Measuring the Atlantic Meridional Overturning Circulation at 26°N, Progress in Oceanography, 130, 91–111, https://doi.org/10.1016/j.pocean.2014.10.006, 2015.

Mercier, H., Desbruyères, D., Lherminier, P., Velo, A., Carracedo, L., Fontela, M., and Pérez, F. F.: New insights into the eastern subpolar 820 North Atlantic meridional overturning circulation from OVIDE, Ocean Science, 20, 779–797, https://doi.org/10.5194/OS-20-779-2024, publisher: Copernicus Publications, 2024.

Nurser, A. J., Marsh, R., and Williams, R. G.: Diagnosing water mass formation from air-sea fluxes and surface mixing, Journal of Physical Oceanography, 29, 1468–1487, https://doi.org/10.1175/1520-0485(1999)029<1468:DWMFFA>2.0.CO;2, 1999.

Petit, T., Lozier, M. S., Josey, S. A., and Cunningham, S. A.: Atlantic Deep Water Formation Occurs Primarily in the Iceland Basin and 825 Irminger Sea by Local Buoyancy Forcing, Geophysical Research Letters, 47, e2020GL091 028, https://doi.org/10.1029/2020GL091028, publisher: John Wiley & Sons, Ltd, 2020.

Rühs, S., Oliver, E. C., Biastoch, A., Böning, C. W., Dowd, M., Getzlaff, K., Martin, T., and Myers, P. G.: Changing Spatial Patterns of Deep Convection in the Subpolar North Atlantic, Journal of Geophysical Research: Oceans, 126, e2021JC017 245, https://doi.org/10.1029/2021JC017245, publisher: John Wiley & Sons, Ltd ISBN: 10.1029/2021, 2021.

830 Speer, K. and Tziperman, E.: Rates of Water Mass Formation in the North Atlantic Ocean, Journal of Physical Oceanography, 22, 93–104, https://doi.org/10.1175/1520-0485(1992)022<0093:rowmfi>2.0.co;2, 1992.

Swingedouw, D., Braconnot, P., Delecluse, P., Guilyardi, E., and Marti, O.: Quantifying the AMOC feedbacks during a 2×CO2 stabilization experiment with land-ice melting, Climate Dynamics, 29, 521–534, https://doi.org/10.1007/s00382-007-0250-0, publisher: Springer, 2007.

Tooth, O. J., Johnson, H. L., Wilson, C., and Evans, D. G.: Seasonal overturning variability in the eastern North Atlantic subpolar gyre: a Lagrangian perspective, Ocean Science, 19, 769–791, https://doi.org/10.5194/OS-19-769-2023, publisher: Copernicus Publications, 2023.

Tsujino, H., Urakawa, S., Nakano, H., Small, R. J., Kim, W. M., Yeager, S. G., Danabasoglu, G., Suzuki, T., Bamber, J. L., Bentsen, M., Böning, C. W., Bozec, A., Chassignet, E. P., Curchitser, E., Boeira Dias, F., Durack, P. J., Griffies, S. M., Harada, Y., Ilicak, M., Josey, S. A., Kobayashi, C., Kobayashi, S., Komuro, Y., Large, W. G., Le Sommer, J., Marsland, S. J., Masina, S., Scheinert, M., Tomita, H., Valdivieso, M., and Yamazaki, D.: JRA-55 based surface dataset for driving ocean–sea-ice models (JRA55-do), Ocean Modelling, 130, 79–139, https://doi.org/10.1016/j.ocemod.2018.07.002, publisher: Elsevier Ltd, 2018.

Tziperman, E.: On the role of interior mixing and air-sea fluxes in determining the stratification and circulation of the oceans, Journal of Physical Oceanography, 16, 680–693, https://doi.org/10.1175/1520-0485(1986)016<0680:OTROIM>2.0.CO;2, 1986.

Wang, H., Zhao, J., Li, F., and Lin, X.: Seasonal and Interannual Variability of the Meridional Overturning Circulation in the Subpolar North Atlantic Diagnosed From a High Resolution Reanalysis Data Set, Journal of Geophysical Research: Oceans, 126, https://doi.org/10.1029/2020JC017130, 2021.

Weijer, W., Cheng, W., Garuba, O. A., Hu, A., and Nadiga, B. T.: CMIP6 models predict significant 21st century decline of the Atlantic Meridional Overturning Circulation, Geophys. Res. Lett., 47, e2019GL086 075, https://doi.org/10.1029/2019gl086075, publisher: Blackwell Publishing Ltd, 2020.

Yang, J.: Local and remote wind stress forcing of the seasonal variability of the Atlantic Meridional Overturning Circulation (AMOC) transport at 26.5N, Journal of Geophysical Research: Oceans, 120, https://doi.org/10.1002/2014JC010317, 2015.

Zhao, J. and Johns, W.: Wind-driven seasonal cycle of the atlantic meridional overturning circulation, Journal of Physical Oceanography, 44, https://doi.org/10.1175/JPO-D-13-0144.1, 2014.